Application of a Bragg Curve Detector to inclusive (p, α) reactions to the continuum

Tshilidzi Thovhogi

A thesis submitted in fulfilment of the requirements

for the degree of Masters in Science

in the Department of Physics

University of Cape Town

March 2003

I declare that, except where acknowledged, the work contained in this thesis to be my own original work, carried out with the guidance and the advice from my supervisor. I also acknowledge the assistance of my supervisor, colleagues and fellow students during the periods when experimental measurements were made, this not being possible to execute except by way of a team.

T. Thovhogi

Signature: .....T. Thovhogi.....

On the ..04th.... *day of* .....June..... *2003*

Application of a Bragg Curve Detector to inclusive (p, α) reactions to the continuum

Tshilidzi Thovhogi[1,2]

[1]UCT, Department of Physics, Private Bag, Rondebosch, 7701, South Africa
e-mail: thovhogi@science.uct.ac.za

[2]*i*Themba LABS, P. O. Box 722, Somerset West, 7129, South Africa
e-mail: thovhogi@tlabs.ac.za

Abstract

The Bragg curve spectroscopy (BCS) technique employed to identify the light mass fragments of proton-induced reactions was described and demonstrated using the Bragg curve detector (BCD). A feasibility study of measuring the continuum emission energy spectra of light mass fragments using the BCD at iThemba LABS has been done for the first time. The application of the BCD and its performance was investigated on proton-induced reactions on ^{12}C at an incident energy of 200 MeV, over an angular range of 30^o to 130^0. The reaction products with atomic numbers of $2 \leq Z \leq 6$ were measured with a BCD down to an energy threshold of about 1 MeV/amu using isobutane as the detector gas. Double differential cross sections of the energy and angular distributions of the emitted α particles were of interest. Comparisons of the experimental angular distribution with a phenomenological approach suggest that the α spectra at low emission energies indicate an increase in the multistep compound contribution to the cross section.

Acknowledgements

I wish to express my sincere gratitude to my supervisor, Dr. R. Fearick and my co-supervisor, Dr. S. V. Förtsch, for their guidance and support throughout the duration of the project.

I am grateful to the DAAD and iThemba LABS, for their financial support.

I am very much indebted to:

- those who assisted during the many weekends of data acquisition: G. F. Steyn, K. Pysz, R. Smit, H. Machner, F. Goldenbaun, M. Kistryn and R. D. Neef.
- G. K. Mabala, for sharing his insight concerning many aspects of the data analysis.

I would like to thank my colleagues and all my friends for their co-operation and support.

Finally, I would like to thank my parents for their support, love, and encouragement.

Tshilidzi Thovhogi, *UCT, March 2003*

Contents

List of Figures

List of Tables

Chapter 1

Introduction

1.1 Overview

The emission of intermediate-mass fragments (IMFs) in reactions induced by energetic protons and heavy ions have been a subject of recent interest [Por89, Cer92]. These measurements are mostly done at higher incident energies above 1 GeV on heavier targets. Kotov et. al. [Kot95] investigates the evolution of the main characteristics of the IMF production process in the wide range of heavier targets from Al to Au with 1 GeV protons. While Porile et. al. [Por89] investigate the IMF produced in the reaction of 1 - 19 GeV protons on a xenon target in which the evolution of multifragmentation is described in terms of a phase transition, similar studies used heavy ions as projectiles such as in the fusion of ^{32}S with ^{107}Ag at an energy of 30 MeV/amu [Cer92]. While the physics concerning the fragmentation of both the target and the projectile still needs to be fully understood a number of applications make use of the experimental cross sections. For instance the study with protons on the heavier targets provide data for the design of spallation sources required for accelerator driven system, that might be used to amongst others burn long-lived nuclear waste.

Due to their low binding energies, IMFs of atomic numbers of $3 \leq Z \leq 5$ (Li, Be and B) are highly unstable and are unlikely to survive the temperature and the pressure encountered during stellar nucleosynthesis. In order to understand

the abundances of these nuclei, spallation reactions induced by protons in nuclei such as ^{12}C, ^{14}N and ^{16}O in low-density astronomical environments and cosmic rays have been proposed. In the case of ^{12}C 50 % of Li, Be and B production are formed by spallation reactions induced by protons on ^{12}C in the cosmic rays. The choice of a ^{12}C target does not lie only in its astrophysical importance [Wes88], but will also provide data for nuclear medicine especially in hadron therapy.

In the present work, the IMFs produced in the interactions of 200 MeV protons with a ^{12}C target are studied. The incident energy of 200 MeV was chosen since the energy spectrum of the protons in the cosmic rays peaks between 100 MeV and 1 GeV and also for medical purposes due to the fact that most of these facilities run with 200 MeV protons. The cross sections for the production of Li, Be and B from spallation of a ^{12}C target were previously studied at an incident energy of 100 MeV [Roc76]. A study at 200 MeV should contribute in an important way to the overall interpretation of the yields previously obtained at lower incident energies.

While formal theories are still being developed to describe the emission of IMF's over a wide range of reactions and energies, data from the (p,α) reaction between 100 and 200 MeV from different target masses as low as ^{27}Al was studied recently [Cow96]. In this study both the statistical multistep (SM) theory and Feshbach, Kerman and Koonin (FKK) [Fes80] theory and the phenomenological prescription of Kalbach [Kal81] was found to reproduce the (p,α) data successfully. Similar calculations with the FKK theory for the reaction ^{12}C(p,α) have not produced consistent results yet. While other models like Intra Nuclear Cascade (INC) [Enk99] are also tested and implemented at these energies to predict also the (p,α) cross sections, the Kalbach systematics are applied in the present study to obtain an indication of the possible reaction mechanism.

The previous (p,α) measurements [Roc76, Cha99] used standard ΔE-E detector telescopes. Since the energy threshold of such a set up depends on the thickness of the ΔE detector, for the first time, at iThemba LABS, a Bragg curve detector (BCD) was used to measure the low energy part of these spectra. With such a detector which uses a thin entrance window energy threshold of about 1 MeV/amu

can be achieved. The BCD has been used widely in other nuclear studies such as multifragmentation [Tan95, Och96]. It is used in intermediate-energy (100 MeV - 1 GeV) nuclear reaction studies, where they provide information on energy and atomic numbers of light mass particles and IMFs. The degree of usefulness of BCD depends on the reliability of the detector gas and the Frisch grid to anode gap to their response in terms of the physical quantities, such as the particle energy and range or atomic and mass numbers.

The present work describes a Bragg Curve Detector (BCD) that realizes all the current identification techniques; i.e. Bragg peak amplitude and range-energy relation [Ort98]. The study of IMF emission in the interaction of 200 MeV protons with a ^{12}C was investigated using a BCD. The application of the BCD and its performance has been investigated by determining the energy and angular distributions of inclusive double differential cross sections of IMFs ($2 \leq Z \leq 6$) at emission energies as low as about 1 MeV/amu.

1.2 Nuclear Reaction Mechanism

1.2.1 Target Fragmentation

In nuclear reactions with light ions of high bombardment energies (about 100 MeV/amu), the initial collision between the projectile and the individual nucleons in the target nucleus is so fast and violent that the first few events results almost always from direct processes. This stage is followed by a series of individual nucleons (or small groups of nucleons) and either IMFs may be ejected (called spallation or fragmentation) or the target may break into several large fragments (called multifragmentation). While the first stage is well described by the INC model [Enk99, Cug97] the later stages regarding fragmentation are treated by the statistical multistep fragmentation model (SMM) as far as medium-weight targets are concerned [Bot90]. Since the projectile was chosen to be a proton IMFs can only originate from the target.

1.2.2 Statistical Multistep Reactions

Figure 1.1 is a schematic illustration of the typical energy spectrum of particles emerging from nuclear reactions. At the upper end of the spectrum are a number of discrete peaks due to elastic scattering, inelastic scattering and transfer reactions. The highest energy peak is the elastic peak, which has the same energy as the incident energy of the emerging particle in the center of mass system. At lower emission energies, the peaks corresponding to more closely spaced levels in final nuclei are not fully resolved because of the detector limitation and spread in energy of the incident beam. At the lower end of the energy scale, we see a broad continuum, below 10 MeV, which is mainly due to decays of compound nucleus. The statistical or compound nucleus model was first proposed by Bohr in 1937. Its basic assumption is the independence of formation and decay of the compound nucleus.

Direct and compound nucleus reactions [Hod71] have been extensively used to analyse a large number of nuclear reactions. But it is also possible for emission to take place after the direct stage and before the attainment of full statistical equilibrium. These are also called pre-equilibrium [Gad92] reactions. At the energies at which these reactions occur the states are strongly overlapping (this region is called the continuum). In order to calculate the pre-equilibrium cross sections, it is necessary to make statistical assumptions. The statistical multistep theory [Fes92] of FKK can also be used to analyse these type of reactions. This theory makes use of the distinction between multistep compound (MSC) and multistep direct (MSD) reactions: in MSC reactions all the particles remain bound during the equilibration cascade, whereas in MSD reactions one particle always remains in the continuum. Figure 1.2 shows the schematic diagram illustrating the distinction between MSC and MSD reactions [Fes92].

The multistep reaction theory is a quantum mechanical theory [Fes95] that provides an analysis of the steps taken in the production of the compound nucleus and extends the direct theory to include many interaction rather than one. As referred to Figure 1.2 the first collision excites a nucleon to a higher shell-model state, thus creating a particle-hole pair. The second collision creates a further particle-hole

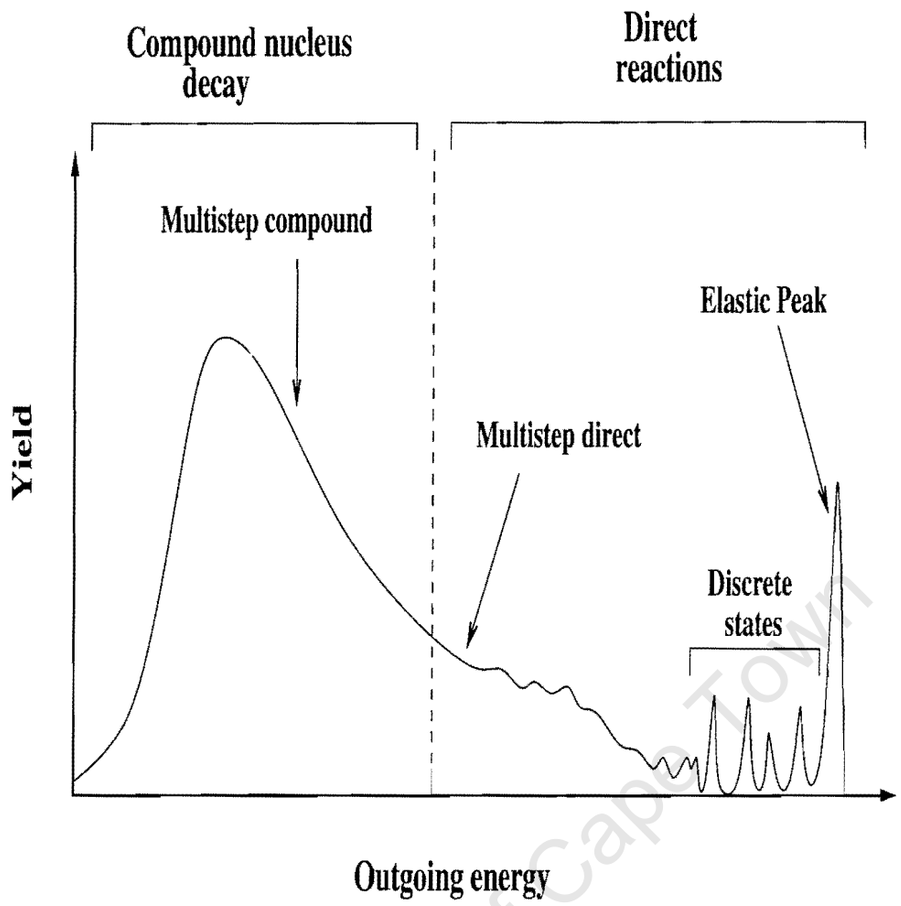

Figure 1.1: *Schematic energy spectrum of particles emitted from a nuclear reaction.*

pair, and the process continues until the energy of the projectile is shared among the nucleons of the target nucleus. At each stage of the collision it is possible for one of the nucleons to gain enough energy to escape from the target nucleus. This process goes for about 10^{-16} s, until the different types of particle are emitted, leaving the residual nucleus in the continuum state or in a particular excited state.

At incident energies of 80 MeV to 200 MeV the statistical multistep model of Feshbach, Kerman and Koonin (FKK) [Fes80, Fes93] has been extensively used

to analyse proton induced reactions such as (p, p′) [Cow90], (p,α) [Cow96] and (p,n) [Tra89]. Kalbach [Kal81] used the basic assumptions of the FKK theory to parameterize the preequilibrium cross sections. These parmeterizations are used as an approach to establish the role which the MSD or MSC processes play in these cross sections.

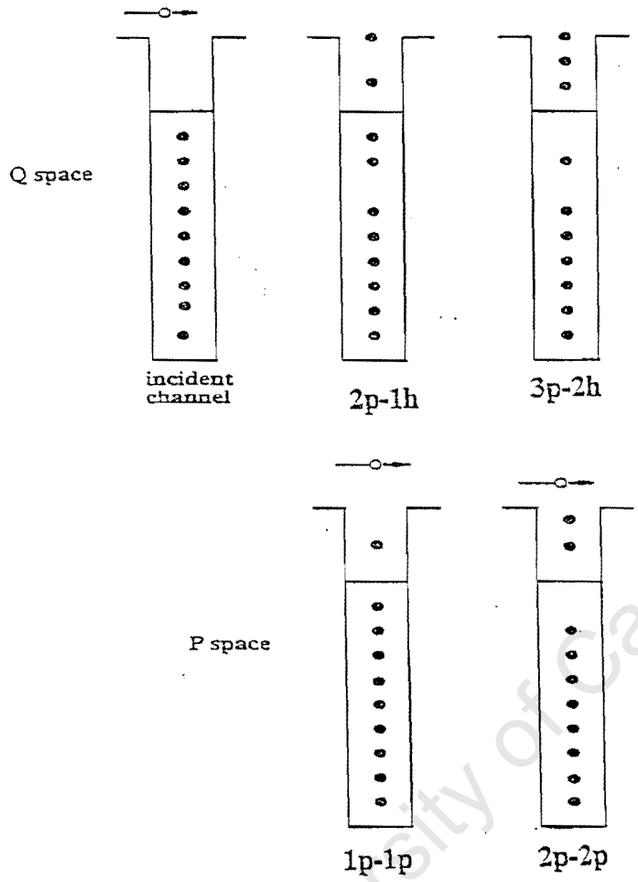

Figure 1.2: *Schematic shell model example of increasing complexity. Here P and Q space are for the MSD and MSC, respectively [Fes92].*

Typical angular distributions for the differential cross sections, in the centre-of-mass, of reaction products from MSD and MSC reactions are shown in Figure 1.3. The angular distribution of the emitted particles from direct reaction and a multistep direct is forward peaked, since the projectile suffers a glancing or peripheral

collision with the target from which the emitted particle will carry most of the incident energy and momentum of the projectile. Hence, the emitted particle will tend to continue moving in the forward direction. The angular distribution of the particles evaporated from a MSC reaction is symmetric about 90 ^{o}, since the compound nucleus stays together sufficiently long enough for its excitation energy to be shared statistically amongst all nucleons so that all memory of its mode of formation is lost. That indeed proves the Bohr independence hypothesis.

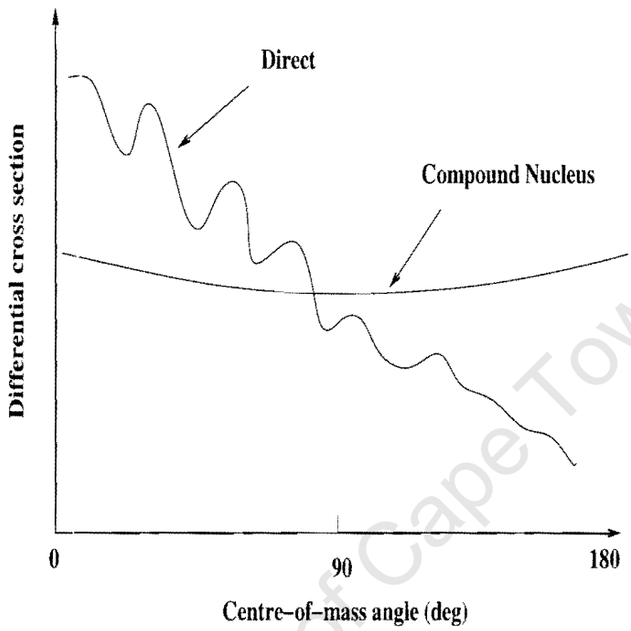

Figure 1.3: *Typical angular distributions for the differential cross sections, in the centre-of-mass, of the particles emitted from direct and compound nuclear reactions.*

1.3 Gas Detectors

Gas detectors are simple to construct and do not suffer from radiation damage. In this section, the basic principles of an ionization chamber and in particular an

axial gridded ionization chamber is described briefly.

1.3.1 Ionization Chamber

The simplest gas detector is an ionization chamber, which measures the ionization produced when charged particles pass through a gas as shown in Figure 1.4. In the central region of the detector where the ionization track is created the incident radiation is perpendicular to the electric field . The resulting voltage pulse shape across the resistor depends on the time taken for the electrons and ions to reach their respective electrodes and the position at which ions pairs were formed within the chamber.

1.3.2 Axial Gridded Ionization Chamber

The dependence of the voltage pulse on position at which ion pairs are formed can be removed by the use of an axial gridded ionization chamber (also called Bragg curve detector), shown in Figure 1.5, which has a fine wire mesh called Frisch grid, placed close to the anode. This serves to screen the anode from the effects of the movement of charge within the active volume of the chamber until the electron reaches the gap between grid and the anode. The electric field is parallel to the incident radiation. The voltage pulse measured between the grid and the anode is determined only by the electron transit time between the grid and the anode. The amplitude of the voltage pulse is proportional to the charge collected. The design and principle of such a detector is described in detail in Chapter 2.

1.4 Interaction of Radiation with Matter

The detection of radiation is based on its interaction with the material of which the detector is made and the energy deposited in this material. This section discusses the mechanism by which ionizing radiation interacts and loses energy as it moves through matter.

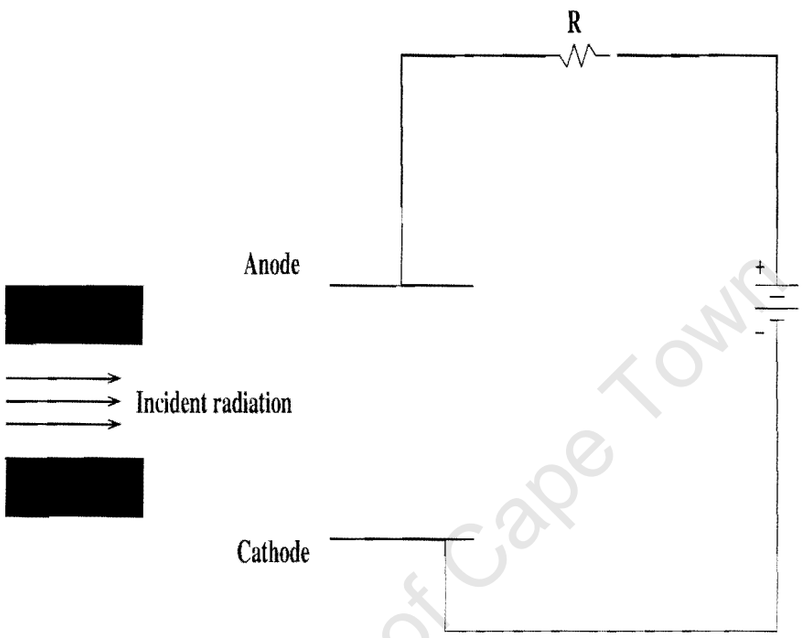

Figure 1.4: *Operational principle of the ionization chamber. All ions must be formed in the lower region of the chamber between the cathode and anode. The electric field is maintained perpendicular to the incident radiation.*

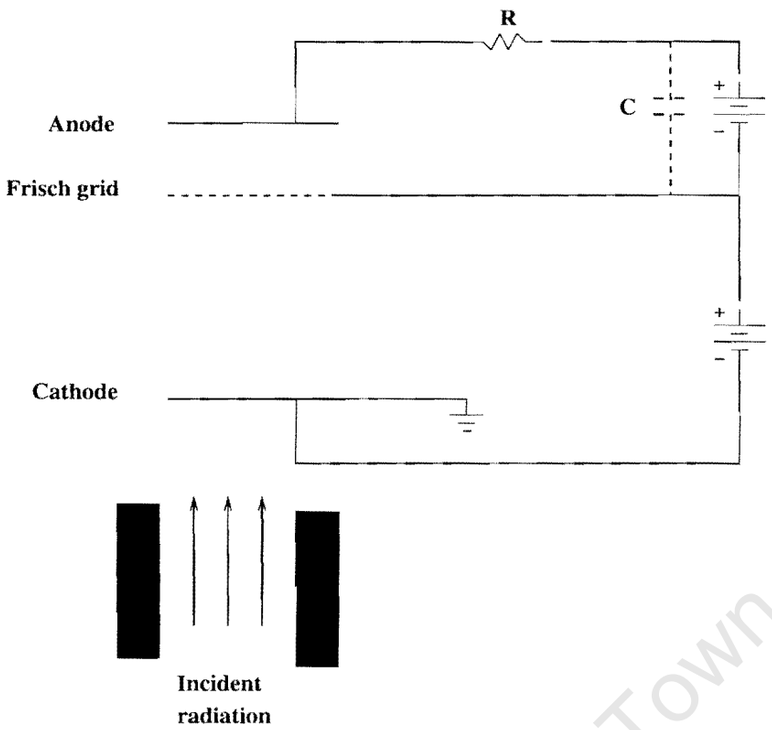

Figure 1.5: *Operational principle of the axial gridded ion chamber. All ions must be formed in the lower region of the chamber between the cathode and grid. The electric field is maintained parallel to the incident radiation.*

1.4.1 Interaction of Heavy Charged Particles

Heavier charged particles, such as the α particle, loses energy via the interaction of its electric field with the atoms it encounters as it passes through matter. They interact with matter primarily through the Coulomb force between their positive nuclear charge and the negative charge of the orbital electrons within the absorber. The products of this interaction in the absorber are either excited atoms or ion pairs. Each ion pair is made up of free electrons and the corresponding positive ion of an absorber atom which an electron has either totally removed through ionization or raised to a higher lying shell through excitation. The energy that is transferred to the electron must come at expense of the kinetic energy of the charged particle, and its velocity is therefore decreased as a result of the encounter [Lil01]. The maximum energy that can be transferred from a charged

particle of mass M with kinetic energy E to an electron of mass m in a head-on collision will be given by

$$\Delta E = 4E\ (\frac{m}{M}). \tag{1.1}$$

The amount transferred in each collision is generally a very small fraction of the particle's total kinetic energy. For a 4 MeV α particle, this is about 2.2 keV.

1.4.2 Stopping Power

The rate at which a particle loses energy per unit path length is known as stopping power of the medium. The stopping power [Kno99] for charged particles in a given absorber is simply defined as the differential energy loss for that particle with the material divided by the differential path length $(-\frac{dE}{dx})$. The value of $-\frac{dE}{dx}$ along a particle track is known as specific energy loss. The quantum-mechanical expression that describes the specific energy loss including relativistic effects, is known as the Bethe-Bloch formula [Tso83]:

$$-\frac{dE}{dx} = (\frac{ze^2}{4\pi\epsilon_0})^2\ \frac{4\pi Z\rho N_A}{Amv^2}\ [\ \ln(\frac{2mv^2}{I}) - \ln(1-\beta^2) - \beta^2\ ] \tag{1.2}$$

where,

$v = \beta c \equiv$ *is the ion velocity*

$ze \equiv$ *its electronic charge*

$m \equiv$ *is the mass of an electron*

$N_A \equiv$ *is Avogadro's number*

$I \equiv$ *is the mean energy required to ionize an atom in the medium*

A, Z *and* $\rho \equiv$ *are the atomic mass number, atomic number and the density of stopping material, respectively.*

1.4.3 Bragg Curve and Particle Range

A plot of the specific energy loss along the track of a charged particle such as shown in Figure 1.6, is known as the Bragg curve. It is characteristic for the way charged particles distribute their energy in matter. Near the end of the path, as the particles loses energy, the ionization density increases steadily until it reaches

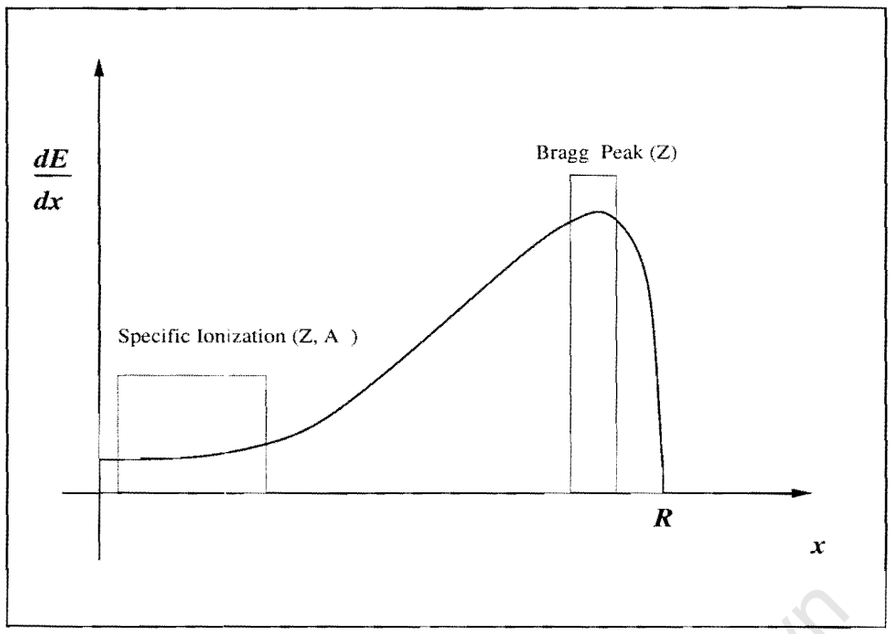

Figure 1.6: *Principle of Bragg curve spectroscopy, where* $\frac{dE}{dx}$ *is the energy loss, R is the range, and A, Z are the mass and charge of the particle respectively.*

a pronounced peak, the so called Bragg peak. Then, it sharply falls down to zero due to electron pick up, enabling the range of the particle to be defined in the medium. The Bragg curve is particularly used in medical applications where it is desired to deliver a high dose of radiation to certain, localized tumours with minimum radiation damage of the overlaying tissue [Leo87].

The range of a charged particle depends on its energy, mass, charge and the nature of the absorber material. Table 1.1 shows the ranges of different charged particles in isobutane of 300 mbar pressure at 25 °C calculated by computer program called TRIM [Bie89] based on equation 1.2.

Table 1.1: *Table showing the ranges of different particles in isobutane at a pressure of about 300 mbar and a temperature of about 25 °C calculated with TRIM.*

Ion	*Ion energy (MeV)*	*Range of ion (mm)*
α	12	153.71
^{7}Li	24	155.64
^{9}Be	36	155.15
^{11}B	50	157.23
^{12}C	60	145.85

1.5 Aim of this Study

The interest of these experiments is mainly in the feasibility of measuring light mass fragments with atomic numbers of $2 \leq Z \leq 6$ produced in the interaction of 200 MeV protons with a ^{12}C target using a BCD at emission energies as low as about 1 MeV/amu. The particular application of a BCD is based on the so called Bragg curve spectroscopy (BCS) method [Gru82]. The BCS technique is based on the fact that the anode signal reproduces the Bragg curve, that is the specific ionization along the track. By handling the digitized Bragg curve, it should be possible, in principle, to identify completely energy, charge and mass of the detected particles.

The original design of the BCD used in this work required the entrance window foil to be made of 2 μm thick aluminized mylar foil. The initial test of the BCD with 200 MeV protons on ^{12}C showed that aluminized mylar foil was not suitable for these types of measurements. The necessary modifications to the entrance window foil which improved the performance of the BCD are presented in detail. Two techniques of processing the Bragg signals were used. The first technique was to use two spectroscopy amplifiers with different shaping times to extract both the particle's charge and total energy. The second technique was to sample and digitize the Bragg signal with the use of a flash ADC.

In Chapter 2 the experimental set-up as well the design and principle of the BCD and the electronics used for data acquisition are described. In Chapter 3 the analysis of the data and the procedure of data taking is described. The experimental results and the Kalbach parameterization results are presented in Chapter 4, while Chapter 5 contains the summary and comments on the next phase of this project.

Chapter 2

Experiment

The initial phase of this experiment was to commission the BCD. The initial test of the BCD with 200 MeV proton beam on ^{12}C target showed that the entrance window foil of the BCD needed to be modified. The neccessary changes made to the BCD will be presented in detail in this Chapter. Subsequently an experiment was performed at iThemba LABS to measure differential cross sections of light mass fragments from proton-induced reactions with a ^{12}C target at incident energy of 200 MeV. The energy and the charge of the fragments with atomic numbers of $2 \leq Z \leq 6$ were determined with the use of a Bragg curve detector over an angular range of 30^o to 130^o in steps of 10^o.

2.1 Bragg Curve Spectroscopy

Particle identification is based on the method of so-called Bragg curve spectroscopy (BCS), which was first proposed by Gruhn et al. [Gru82].

When a particle loses energy and eventually stops in the active volume of the detector as discussed in section 2.2.4 , the resulting energy loss distribution $(\frac{dE}{dx})$ along the ionization path is characterized by the Bragg curve. The Bragg curve contains all the information about the energy, range and the nuclear charge of the ionizing particle.

A typical Bragg curve is shown in Figure 1.6. The maximum of the Bragg curve

amplitude the so-called Bragg peak corresponding to the maximum of the energy loss at the end of the track, is a direct measure of the nuclear charge *(Z)* of the particle. The integral over the Bragg curve gives the kinetic energy *(E)* of the registered particle. The full length of the Bragg curve corresponds to the range *(R)* of the particle and depends on the energy, charge and mass of the particle. A partial integration of the Bragg curve provides an energy loss signal *(ΔE)*, which also depends on the energy, charge and mass of the particle.

2.2 Bragg Curve Detector

2.2.1 Introduction

Previous studies of multifragmentation processes show [Tan95, Och96] that such detectors are able to identify isotopes from Li to Ti with threshold of about 1 MeV/amu. The energy threshold of the BCD is determined by the thickness of entrance window foil. Thin entrance window foils are used in the BCD which imply that the dead layer on the entrance window is almost negligible so that the detector is able to identify low energy of detected particles. Compared with a standard ΔE-E silicon telescope the following advantages appear:

- insensitivity to radiation effects,
- large solid angle is easily achieved,
- adaptation to the energy range by changing gas pressure,
- insensitivity to minimum-ionizing particles, and consequently, the passage of these particles through the detector does not affect the registration of other particles.

2.2.2 Detector Construction

The Bragg curve detector was designed, built and optimized by the detector laboratory of the Institute of Physics, Jagellonian University in Cracow and Institut für Kernphysik (IKP) in Jülich. The construction of the detector is shown in Figure 2.1.

The detector is a stainless steel cylinder 200 mm long and with a 55 mm internal diameter. The entrance window must be as thin as possible in order to minimize the energy loss of incoming particles. The particle enters the detector through a 2 μm thick aluminized mylar foil which constitutes the cathode. It was supported on the outside by a wire mesh. The aluminium layer was used to make the window electrically conductive so that a uniform electric field could be effectively achieved on the surface. The foil thickness was tested to withstand an inner pressure of about 460 mbar. The entrance window design was similar to that of Farrar et. al. [Far94]. The voltage between the cathode and Frisch grid was divided by a resistor chain of 10 MΩ each connected to 7 field shaping rings which preserve the homogeneous longitudinal electric field over the active volume of the detector. The distance between entrance window and Frisch grid was 160 mm, the spacing between grid and anode was 20 mm. The Frisch grid consists of 20 μm tungsten wires with 1 mm spacing. A circular copper disk formed the anode. The cathode and anode voltages were set to be -2500 V and +700 V respectively while the Frisch grid was grounded.

2.2.3 Frisch Grid

The Frisch grid defines the sampling region and is made to be as transparent as possible to the electrons. The sampling region is the gap width between Frisch grid and anode. The sampling region determines the dynamic range of particles which are identified by the Bragg Curve detector. The screening inefficiency to Frisch grid is 1 %. The formula to calculate the screening inefficiency in grid ionization chamber can be written by [Bun47]

$$\sigma = \frac{d}{2\pi p} \log(\frac{d}{2\pi r}) \tag{2.1}$$

where,

$\sigma \equiv$ *screening inefficiency*

$d \equiv$ *wire to wire distance*

$r \equiv$ *wire radius*

$p \equiv$ *distance from grid to anode*

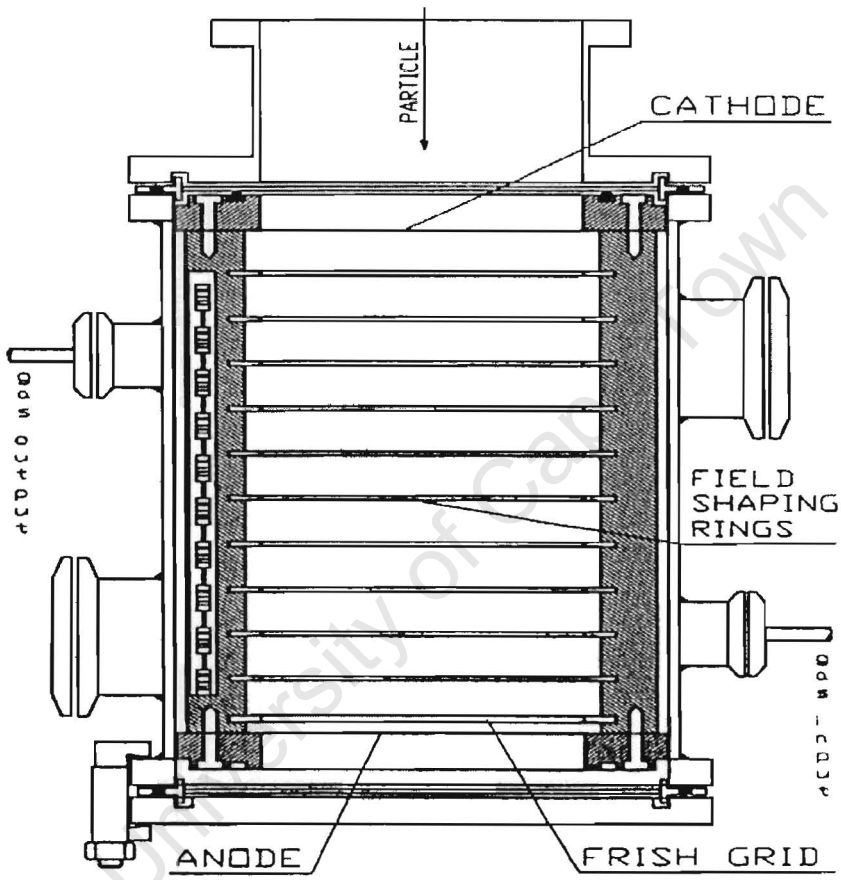

Figure 2.1: *Design of the Bragg curve detector for detection of the spallation reaction products. The distance between the cathode and the anode is 180 mm and with an internal diameter of 55 mm.*

The charge resolution of the Bragg Curve detector depends on the sampling region and the detector gas [She85]. If the range of a particle is shorter than the spacing between Frisch grid to anode, it will not be efficiently detected. Therefore, a careful selection of the Frisch grid to anode distance and the detector gas is necessary, if good charge resolution is required. The proper choice of sampling region depends on the experimental requirements and also on the detector gas. For these measurements 2 cm was chosen based on similar experiments [Mor84].

2.2.4 Principle operation of the Bragg curve detector

A charged particle enters the detector through the thin entrance window, ionizes the gas in the active volume of the detector in which ion pairs are created along its ionization track, and eventually stops after losing all its kinetic energy. The electric field in the gas is maintained parallel to the axis in the central region of the detector where the ionization track is created. Under the action of an electric field ion pairs created in the active volume of the detector split into positive ions and electrons, with the electrons drifting towards the anode while the positive ions drift towards cathode at a smaller rate.

The detector is filled with isobutane $(C_4H_{10})_n$ gas of 99.9 % purity. Based on similar experiments [Ass82] the operation pressure had been chosen to be about 300 mbar. Isobutane is an attractive gas for gas detectors because of its high rate of energy loss per unit gas pressure allowing thin entrance window to be used in the chamber [Jam83]. Based on energy loss and range of the particles calculations, Figure 2.2 shows the performance of isobutane gas against argon gas under the same conditions. The isobutane gas gives higher stopping power than argon gas, hence, a BCD filled with isobutane allows for a short active volume (cathode to anode distance).

The induced current across the anode is proportional to the total number of electrons contained in the grid to anode gap at any given time and is given by [She85]

$$i(t) = \frac{v^-}{d} \int_d^{d+l} q^-(x,t)dx \tag{2.2}$$

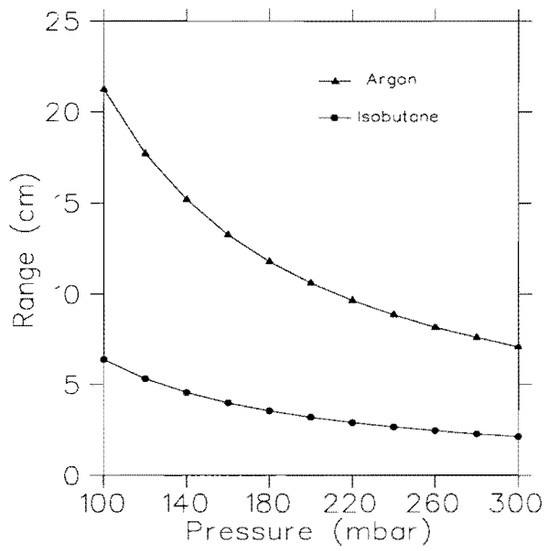

Figure 2.2: *Comparison of the range distribution of 10 MeV ^{10}B ions in argon and isobutane at $T = 20°C$.*

where,
$l \equiv$ *cathode to Frisch grid distance*
$d \equiv$ *Frisch grid to anode distance*
$v^- \equiv$ *drift velocity of an electron*
$q^-(x,t) \equiv$ *ionization charge distribution of an electron at given time*

The anode current $i(t)$ is a representation of the Bragg curve of the ions being stopped in the Bragg curve detector. From Figure 1.5 the voltage signal across the resistor is time-dependent [Kno99] and is given by

$$V_R = \frac{n_0 e}{dC} v^- t \tag{2.3}$$

where,
$n_0 \equiv$ *number of ion pairs*
$e \equiv$ *electron charge of an electron*
$C \equiv$ *capacitance of the detector*

In real practice the voltage signal is across the charge-sensitive preamplifier. This voltage signal increases linearly with time along the track inside the sampling space

(grid-anode space) as shown in Figure 2.3 and, hence the maximum voltage signal is therefore,

$$V_{max} = \frac{n_0 e}{C} \tag{2.4}$$

Since the electron passes through the same potential difference and contributes

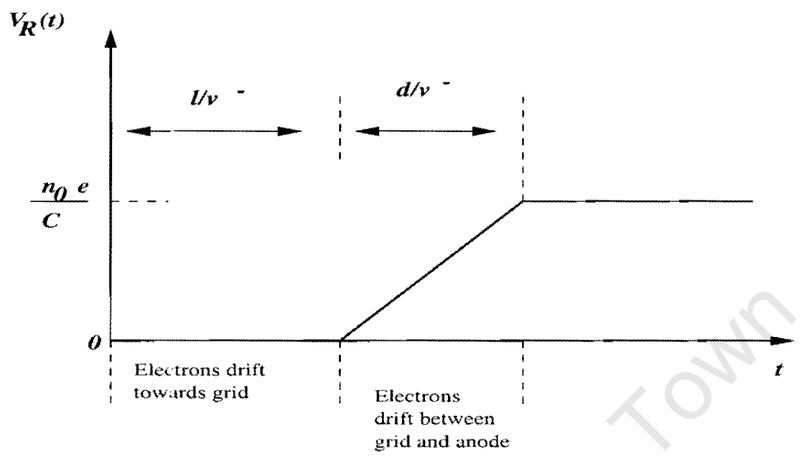

Figure 2.3: *The pulse shape that results from the formation of n_0 ion pairs at a distance l from the grid, where d is the grid-anode spacing [Kno99].*

equally to the signal pulse, the pulse amplitude is now independent of the position of the formation of the original ion pairs and is simply proportional to the total numbers of ion pairs formed along the track of the incident particles.

2.2.5 Detector set-up

The detector was mounted on one of the two rotating arms inside the A-line scattering chamber and covered an angular range of 30^o to 130^o with 10^o steps as shown in Figure 2.4. The angles less than 30^o could not be reached due to its width and length of 55 mm and 200 mm, respectively. The BCD was placed 320 mm away from the target ladder (see Figure 2.5). The geometry considerations for the collimator opening were chosen in such a way to ensure that the particle in the detector creates the ionization track inside the electric field defined by the

field shaping rings. Such a geometry is shown in Figure 2.5 in which a radius of collimator of about 11.5 mm was considered such that the emerging particles are always within the field shaping rings of the detector. The resulting solid angle *($\Delta\Omega$)* is calculated from equation

$$\Delta\Omega = \frac{\pi r^2}{x^2} \tag{2.5}$$

where r (= 11.5 mm) and x (= 217 mm) are the radius of the collimator and the distance from the target to the end of the collimator, respectively. The values of $\Delta\Omega$ was found to be 8.755 $\pm$ 0.042 msr. The collimator was made of brass with a diameter of 23 mm and a thickness of 55 mm. This thickness was chosen to stop 200 MeV protons.

2.2.6 Gas Handling

For good performance of gas-filled detectors the amount of gas in the detector volume must be kept constant, and a reliable system for regulating the pressure and gas flow is needed. The sketch shown in Figure 2.6 is the gas pressure regulation system used for filling the Bragg curve detector with isobutane.

The main procedures which were followed in the gas filling are described as follows. The first step was to open the by-pass allowing the Bragg curve detector to be at the same pressure as the scattering chamber. Because of the thin entrance window of the detector, slow pumping down of the chamber and detector was ensured by slowly opening the throttle on the roughing pump in order to avoid sudden strain on the entrance window of the detector. As soon as the vacuum reached the required pressure for the experiment, the Bragg curve detector was isolated from the scattering vacuum system by closing the by-pass.

Charged particles which enter the detector ionize the gas and create ion pairs. Heavy ions are strongly ionizing particles creating a dense plasma of ion pairs along their path. This plasma reduces the electric field intensity which hinders the drifting of the electrons, thereby increasing the probability of recombination, and lowering in the detector efficiency. Therefore, the gas needs to be replaced

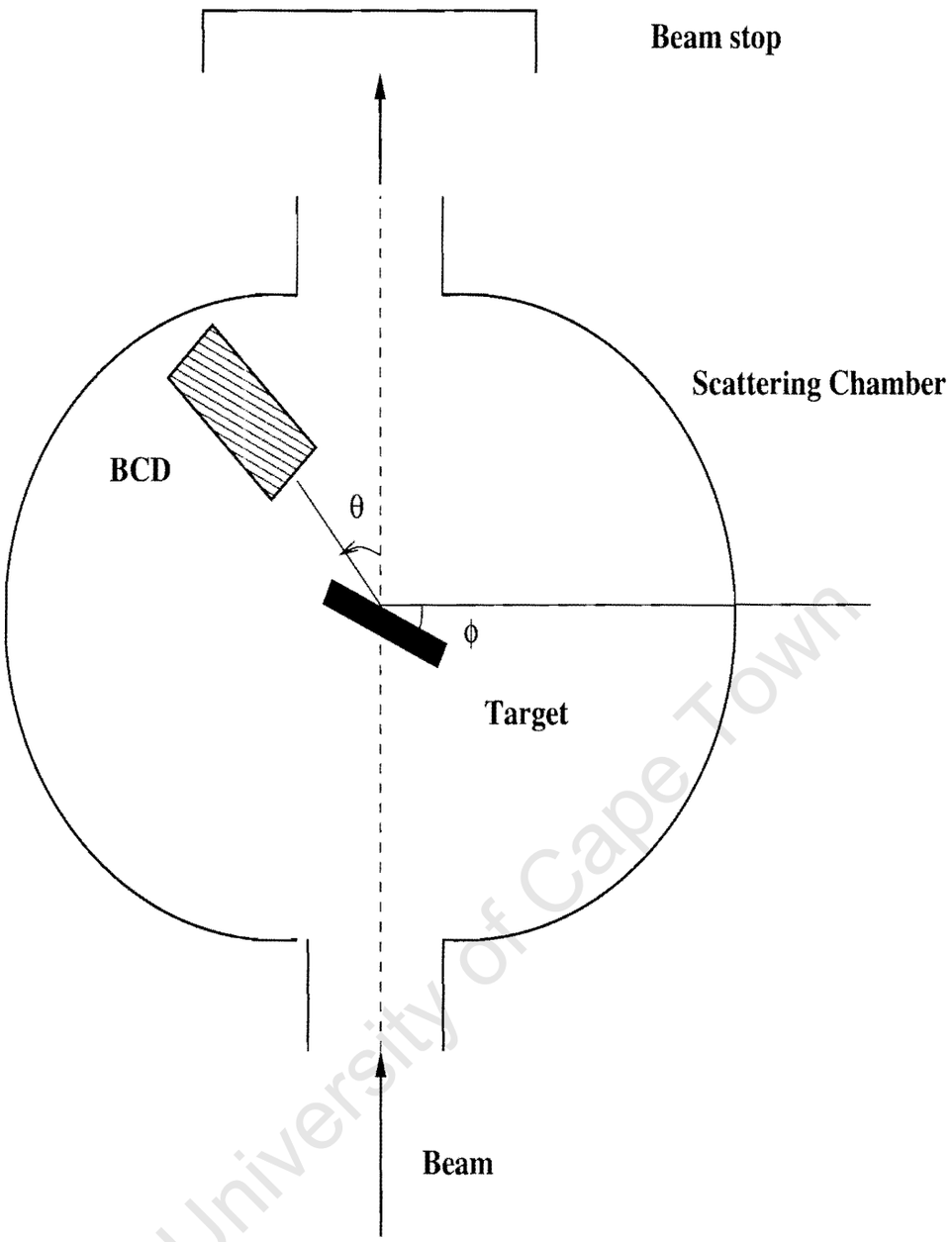

Figure 2.4: *Schematic representation of the detector and target geometry inside the scattering chamber, where θ and ϕ present the BCD angle and the target angle with respect to the beam axis, respectively.*

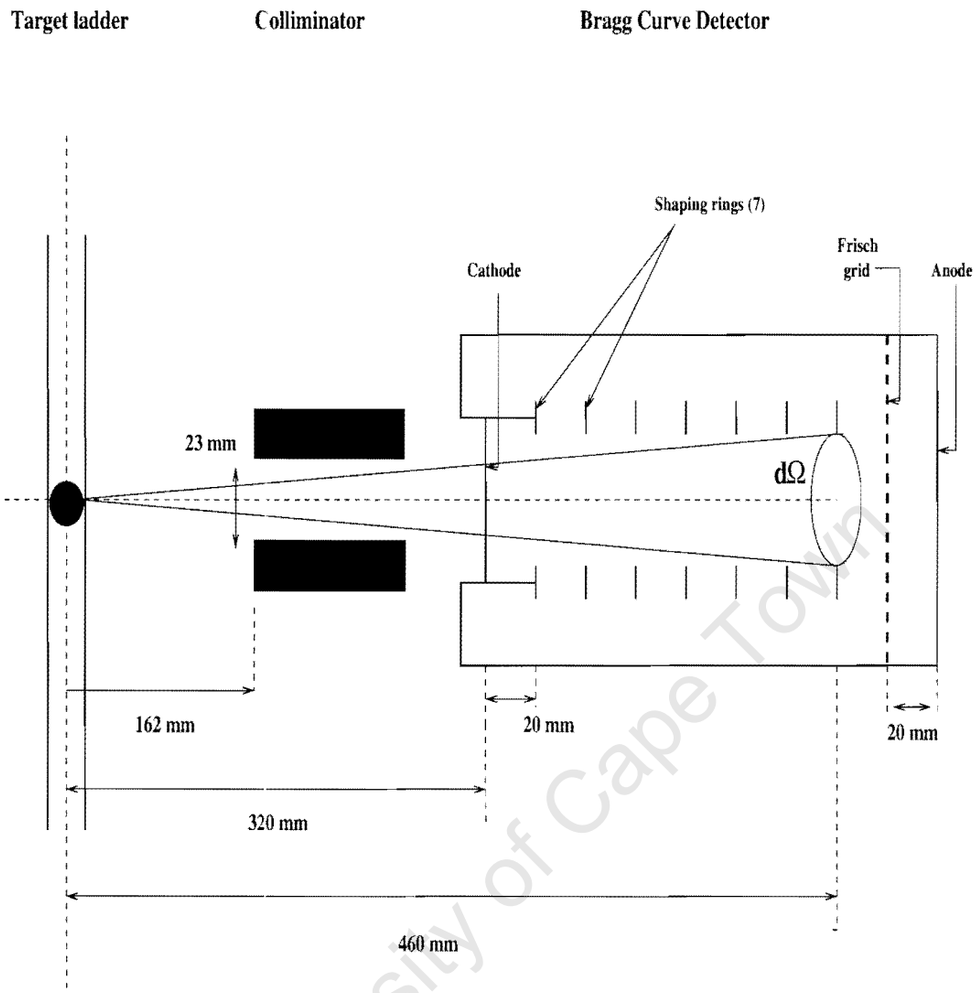

Figure 2.5: *Horizontal representation of the detector set-up inside the scattering chamber with respect to the target, collimator respectively, used to define the solid angle configuration, where $d\Omega$ is the solid angle.*

continuously. A second roughing pump (see Figure 2.6) was included in order to circulate the gas through the BCD.

Once the system was evacuated, the detector was filled with isobutane. The second roughing pump on the outlet of the BCD was then started. Thereafter, the gas bottle valve was opened very slowly until the pressure on the regulator gauge reached about 300 mbar. The gas was then transported to a regulator via a needle valve. Finally, the gas pressure in the regulator was set very slowly to about 300 mbar. The flow rate through the detector was controlled by a needle valve on the second roughing pump. After filling the detector inside the experimental vault the gas regulator system was set to remote in order to have control in the data room. The gas pressure was regulated at 300 mbar throughout the experiment.

2.3 Proton Beam

The iThemba LABS cyclotron facility is a multidisciplinary institute providing beams for basic nuclear physics research, isotope production and radiotherapy for the treatment of benign and malignant growths.

A layout of the facility is shown in Figure 2.7. The maximum beam energy that may be accelerated from the solid-pole-light-ion injector cyclotron (SPC1) depends on the particular beam energy of interest. For a beam of 200 MeV protons the SPC1 accelerates the protons up to a maximum energy of 8 MeV. These 8 MeV protons are then injected into the separated-sector cyclotron (SSC) in which the protons are accelerated to a maximum energy of 200 MeV. The 200 MeV protons were transported via the high-energy beam lines and delivered to the A-line scattering chamber.

2.4 Scattering Chamber

Most light-ion experiments are performed in the iThemba LABS 1.5 m scattering chamber originally acquired from the University of Maryland's Cyclotron laboratory [Raa87]. A vacuum pressure in the order of 10^{-5} mbar can be achieved.

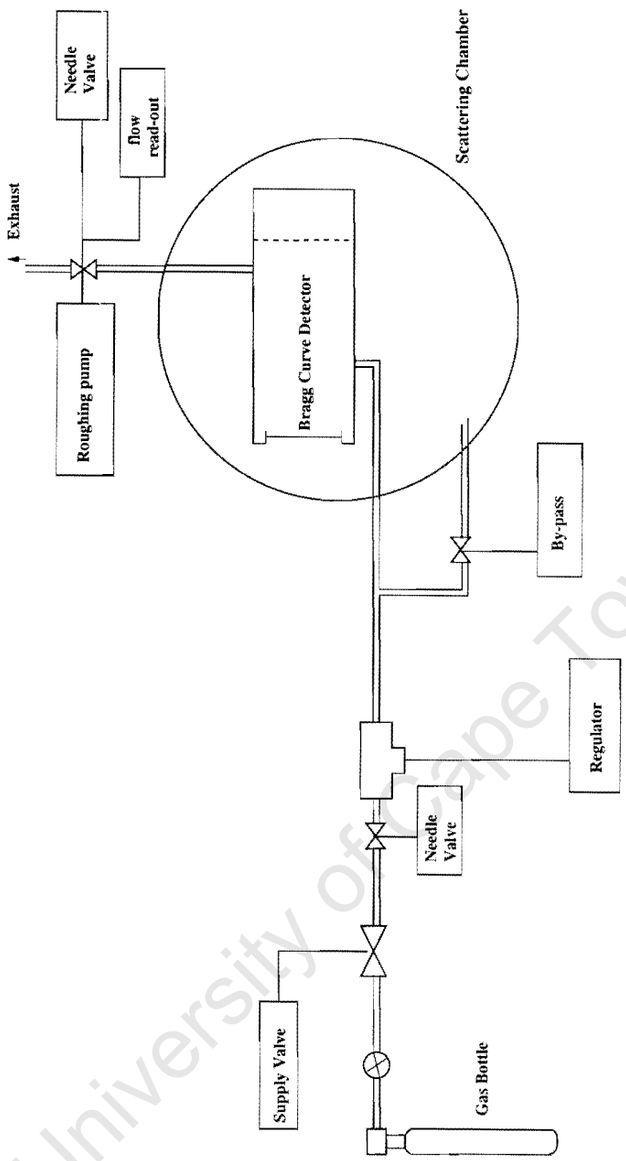

Figure 2.6: *Control system for gas filling.*

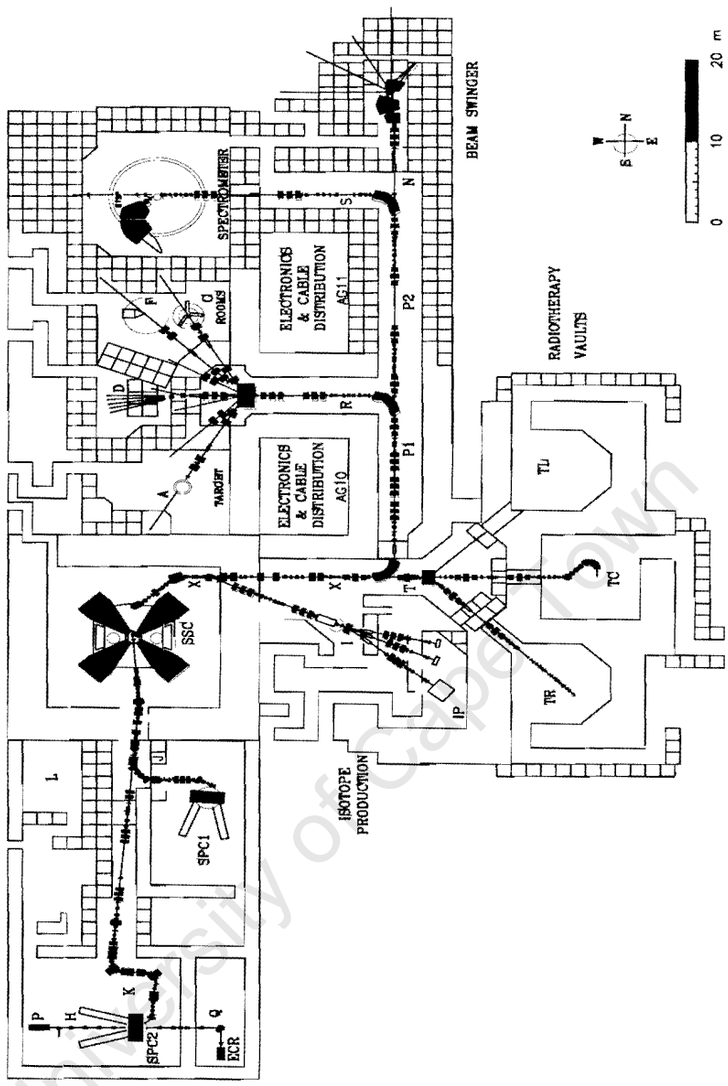

Figure 2.7: *Layout of the iThemba LABS cyclotron facility.*

The target mechanism mounted at the center of the chamber makes provision for five target positions which may be driven vertically so that any of the different targets may be positioned in front of the beam. The target ladder may be also moved to different angle with respect to the beam. The movement of the target ladder has a vertical and angular accuracy of ± 0.25 mm and $\pm 0.1^{\circ}$, respectively

There are two independently movable arms which can be positioned at different angles with respect to the beam. All four movable components namely the upper arm, lower arm, target angle and target height may be controlled and monitored either locally or remotely in the data room.

The chamber has several ports which are used for various purposes. One of these ports which is in the lid of the chamber is used as a window enabling a closed circuit television camera to view the position of the target and for the beam alignment by centering the beam spot into the ruby target. The other ports have cable feedthrough for different cables which to the data room are used for cables connected to the data room via a patch panel.

2.5 Target

The target ladder at the center of the scattering chamber makes provision for mounting five target holder frames. All targets namely ^{12}C, empty, ruby were mounted on the frames of 20 mm in diameter. The ruby with 3 mm hole in diameter was used for tuning a finely focused beam spot at the central position, an empty frame for background minimization purposes and the thin self supporting ^{12}C target of thickness 140 $\mu g/cm^2$.

2.6 Electronics

Two techniques of processing the Bragg signals were employed. The first technique was to use two spectroscopy amplifiers with different shaping times to process the Bragg curve signals such that only the amplitudes of the Bragg signals of each

spectroscopy amplifier are digitized by standard NIM ADCs. The second technique was to sample and digitize the full Bragg signal with the use of a flash ADC.

2.6.1 Detector signals and Preamplifier

A charge sensitive preamplifier amplified the anode signals of the Bragg-curve detector. The distance between the Bragg-curve detector and preamplifier was kept as short as possible to reduce electronic noise pick-up. It was, therefore, placed inside the scattering chamber, strapped to the arm on which the detector was mounted. The preamplifier has a timing and an energy output. Since the Bragg-curve detector produces very slow time signals the energy output signals were used for both for the energy and timing measurements.

2.6.2 Logic Signals

(i) Timing signals for Standard NIM ADC

The timing signals from the energy output signals of the charge sensitive preamplifier were shaped and amplified by a TFA and fed into the CFD. The CFD generates a logic signal at a constant fraction of the peak height to produce an essentially walk-free timing signal [Leo87]. A block diagram representing the logic signal processing is shown in Figure 2.10. The timing signals were used to generate the event trigger and to open the respective ADC gates. Various NIM modules used to process the timing signals, are summarized in Table 2.1.

Table 2.1: *NIM modules for timing signals [2.10].*

Modules	*Model*
Time Filter Amplifier (TFA)	ORTEC 474
Constant Fraction Discriminator (CFD)	ORTEC 436
Logic Fan-in/Fan-out	LeCroy 4287
Gate and Delay Generator (GDG)	ORTEC 416A
4-Fold Logic Unit (4-FLU)	LeCroy 365AL
Dual Gate Generator (DGG)	LeCroy 222

(ii) Timing signals for flash ADC

The timing signals from energy output signals of the charge sensitive preamplifier were fed into a TFA. As illustrated in Figure 2.11 the output from TFA was fed into a CFD. The timing signals were used to generate the event trigger and the stop signals. The delay on the stop signals were set in such a way that they arrive 1-2 μs after the end of the Bragg signals as shown in Figure 2.8. The stop signals were used to alert the flash ADC to sample and digitize each Bragg signal into 200 samples at a clock rate of 10 MHz when the stop signals arrive. The length of the Bragg signal was about 8-10 μs.

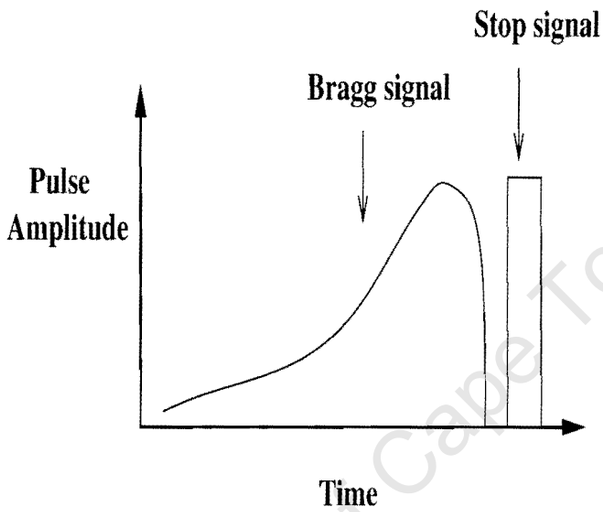

Figure 2.8: *A diagram showing the position of stop signal with respect to the Bragg signal.*

2.6.3 Linear signals

The energy information for each signal was obtained by processing by linear signals. The NIM standard ADCs were used to digitize only the amplitude of the pulse shape registered by the spectroscopy amplifier in the region defined by ADC gates. A flash ADC was used to digitize the full pulse shape registered by the spectroscopy amplifier. The various NIM modules used to process the linear signals for both flash ADC and NIM standard ADC, are summarized in Table 2.2.

Table 2.2: *NIM modules for linear signals.*

Modules	*Model*
Preamplifier	CANBERRA (Preamp) 2005
Spectroscopy Amplifier (Amp)	CANBERRA 2020
Delay Amplifier (Delay Amp)	ORTEC 427A
Analog-to-digital Conveter (ADC)	CANBERRA 8077
flash Analog-to-digital Converter (flash ADC)	CAEN V729A

(i) Standard NIM ADC

In the standard NIM ADC method, two spectroscopy amplifiers each with a different shaping time of 10 μs and 0.25 μs respectively were used to register the pulse shape of the output of a charge sensitive preamplifier. The short shaping time of 0.25 μs, which is approximately equal to the electron transit time between the Frisch grid and the anode, yields information on the Bragg peak, and the long shaping time of 10μs corresponds to the total energy of a particle. A block diagram of the linear electronic for Bragg curve detector illustrating this technique, is shown in Figure 2.9 and Figure 2.10. The analog signals from the amplifiers were digitized with the use of Canberra ADC.

(ii) Flash ADC

The Bragg-curve detector is the detector that realizes all current identification techniques; i.e $\Delta E - E$ separation, Bragg peak amplitude and range-energy relation [Ort98]. A new electronic processing method for this detector which can give such relations has been developed. It is based on the digitization of the pulse shape of the Bragg-curve detector signal with a flash-ADC. The electronic readout of this method which has been published by Ortlepp et al. [Ort89] is also used in the present work.

The Bragg signal from the charge sensitive preamplifier was fed into spectroscopy amplifier. The shaping time of spectroscopy amplifier was set to be 0.25 μs. Then, as illustrated in Figure 2.11 the output signal from the spectroscopy amplifier was

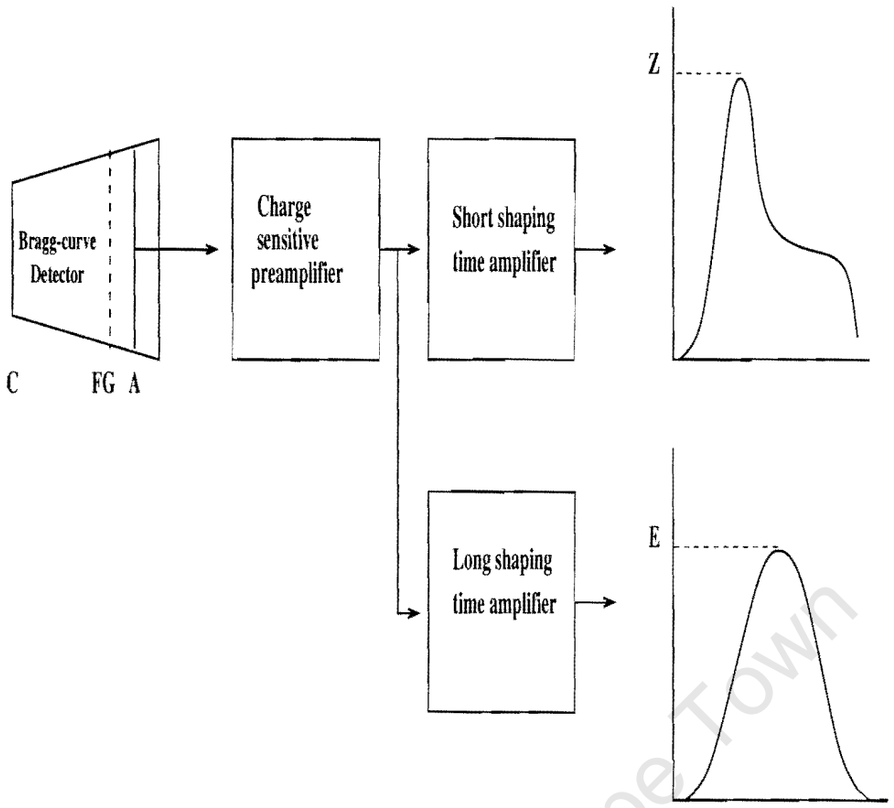

Figure 2.9: *Principle of using two shaping amplifier to process the Bragg-curve signals. Where, C-cathode, FG-Frisch grid, A-anode.*

digitized by a CAEN V729A 12-bit flash-ADC. The CAEN V729A model is a 4 channel 40 MHz ADC housed in a 1-unit wide VME module [CAE99]. This module has three different clock rates, i.e. 10 MHz, 20 MHz and 40 MHz.

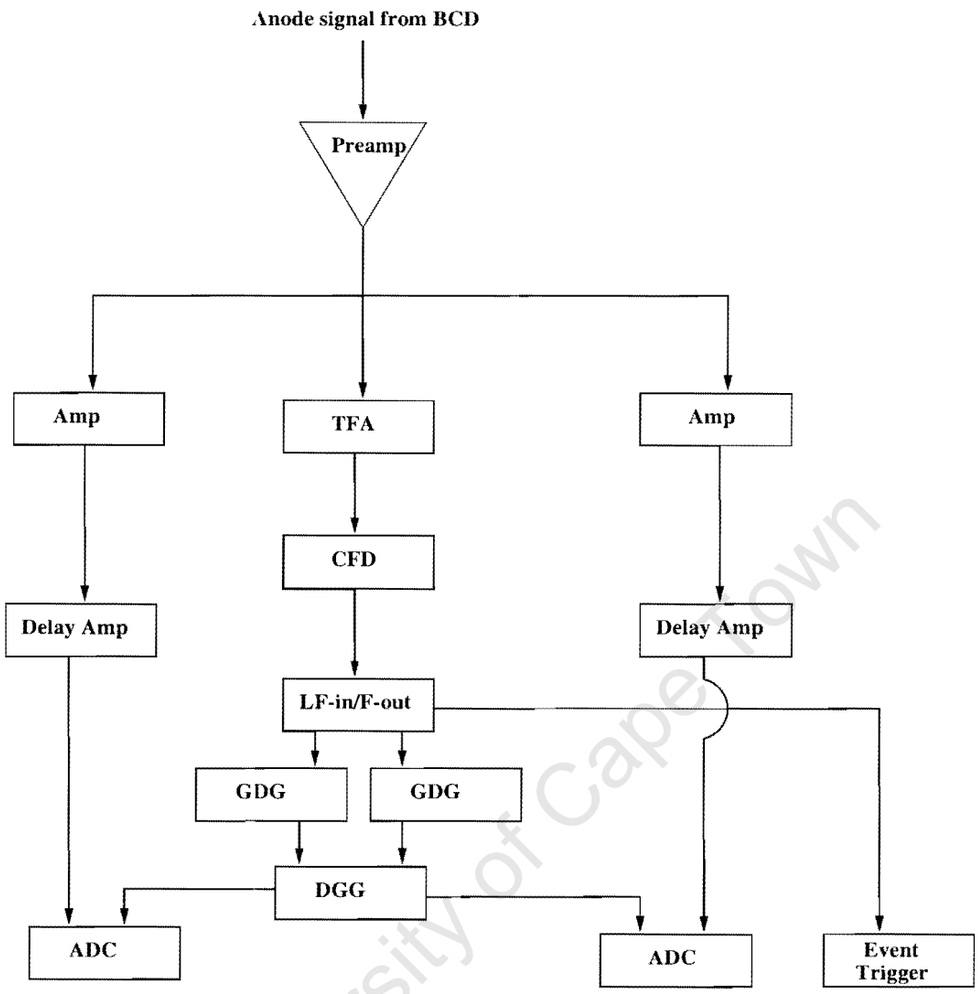

Figure 2.10: *Schematic representation of the measuring electronics (standard NIM ADC) used to process the Bragg-curve detector signals.*

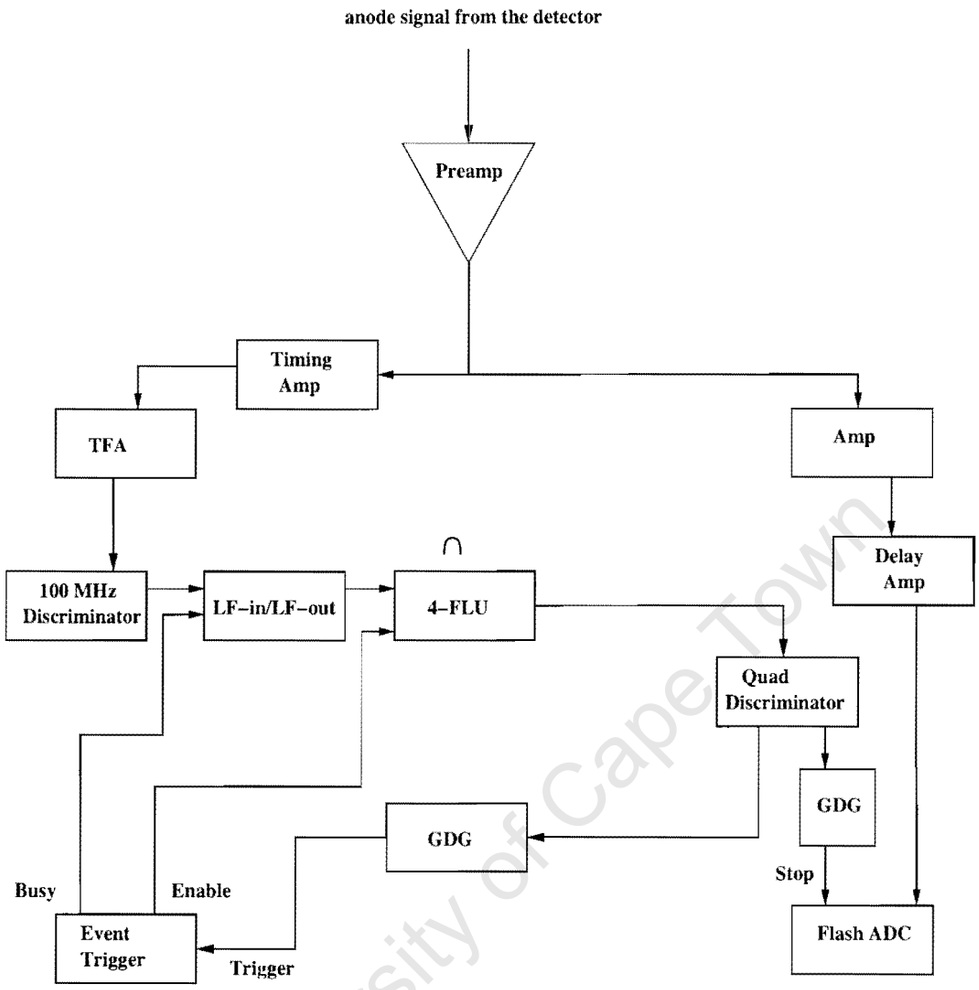

Figure 2.11: *Schematic representation of the measuring electronics (Flash ADC) used to process the BCD signals.*

2.6.4 Clock

The stop output connected to a prescalar (Timer with stop output is connected to start input), was fed into a Timing SCA by which the computer dead time can be monitored. The output from the Timing SCA was sent via discriminator to two CAMAC scaler modules (uninhibited scaler and inhibited scaler that was inhibited by computer busy) as shown in Figure 2.12. The differences of these two scaler reading indicates estimate the computer dead time.

2.6.5 Current Integrator

The proton beam current measured by the beam stop components was fed to Brookhaven Instruments current integrator (BIC model 1000C) module. This module outputs digital pulses with a width of 5 μs [Pil89]. The electronic read-out module of the current integrator was built and developed at iThemba LABS. It allows the selection of the current integrator range which determines the number of pulses output per unit of accumulated charge and its display system enables the position of the selected range to be read by the computer via a CAMAC interface during data acquisition.

2.6.6 Pulsers

An output signal from the current integrator was fed to a prescalar (Timer). The two outputs of the prescalar were fed into the input of a CAMAC scaler module while the other one was sent into Logic fan-in/fan-out. The pulser from the pulse tail generator was triggered at the rate of the beam intensity. The logic fan-in/fan-out was in coincidence with a busy signal from the CAMAC trigger module. This pulser was inhibited whenever the computer was busy and form an inhibited signal to the CAMAC scaler module. Another pulser signal triggered the tail pulser generator which sent the signals to the test input of the the preamplifier. As part of the detector signals stream the pulser signals were also processed by the electronics as discussed in section 2.6. Figure 2.12 shows the block diagram of this setup. The pulser was used to estimate the electronic dead time. The ratio of the pulser events from the ADC to the inhibited pulser from CAMAC scaler module gives the electronic deadtime.

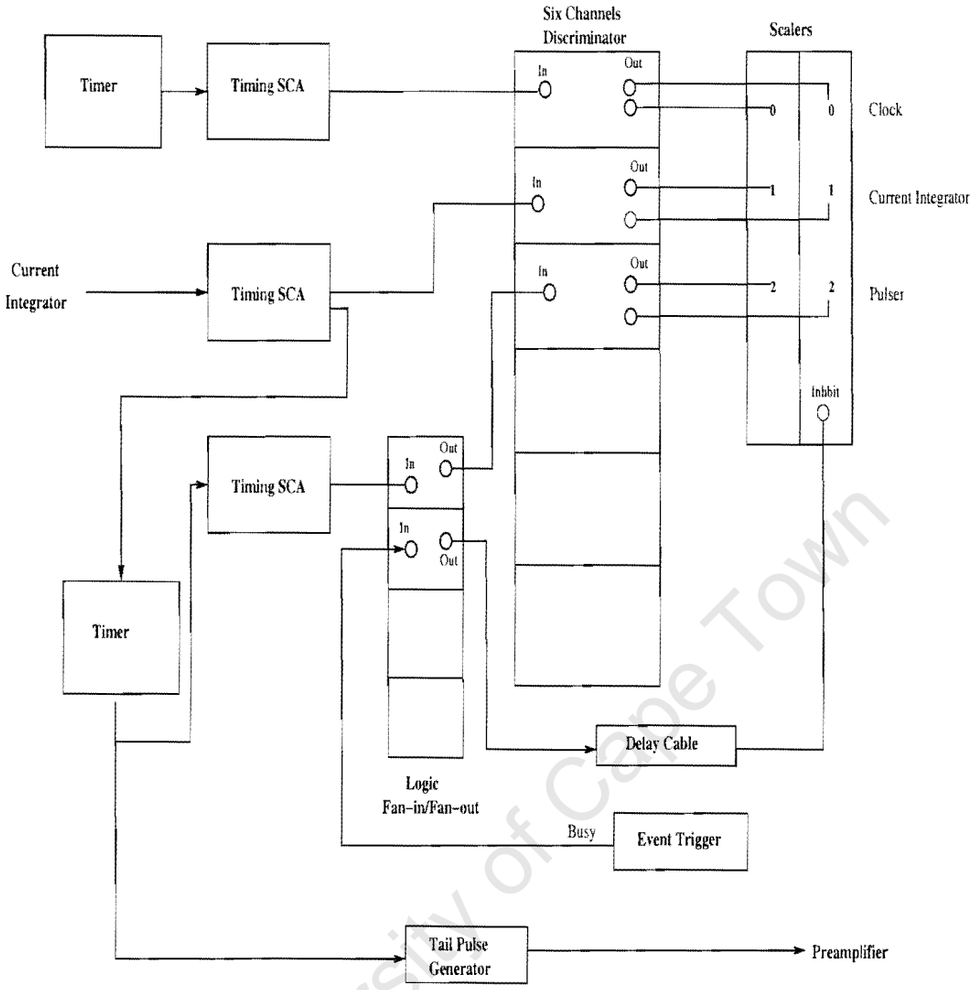

Figure 2.12: *Schematic representation of the electronics used to measure the deadtime and the integrated beam.*

2.6.7 Test of the Bragg Curve Detector

(i) BCD tests with ^{228}Th α source and 200 MeV proton beam

The BCD was tested using a ^{228}Th α source and also with a 200 MeV beam of protons bombarding a 140 μg/cm^2 ^{12}C target. These tests were performed using the design of the BCD described in section 2.2.2. After focusing the beam on target, particle identification spectrum (PID) which is able to differentiate the atomic numbers of different particles was obtained imediately. Such a PID spectrum is shown in Figure 2.13. After running the BCD for a day with beam, the BCD was not able to produce signals carrying any Bragg information. This is indicated in the PID spectrum shown in Figure 2.14 which differs from Figure 2.13 where the different atomic numbers were no longer differentiated. After following up possible causes like the detector gas, preamplifier and power supplies it was found that the aluminized mylar window showed damage to the aluminium layer, especially around the copper contact caused mainly by electrical discharge. The damage to the aluminium layer around the copper contact is indicated by an arrow in Figure 2.15. Hence, the cathode had no electrical contact. The absence of the cathode as an initial field-shaping component of the BCD was confirmed by reducing the gas pressure inside the detector from 300 mbar to 100 mbar. At this lower pressure and shorter dynamic range of the BCD, the signals were found to have Bragg information as shown in Figure 2.16. Clearly the BCD needed to be modified. Possible changes were investigated namely to either ground the entrance window [Och96] and protective grid or to use a separate foil inside the detector as the cathode [Mor84].

It should be noted that these discoveries would have been almost impossible to make with a ^{228}Th source only. Signals associated with different energies and charges of the detected particles were required which was only possible by conducting these tests with beam.

(ii) Modification of the BCD construction

A 1.1 μm thick mylar foil, coated on the inside surface with 2.6 μm thick carbon to make the window electrically conductive, was used as the entrance window instead of 2 μm thick aluminized mylar foil. The anode and the Frisch grid voltages were

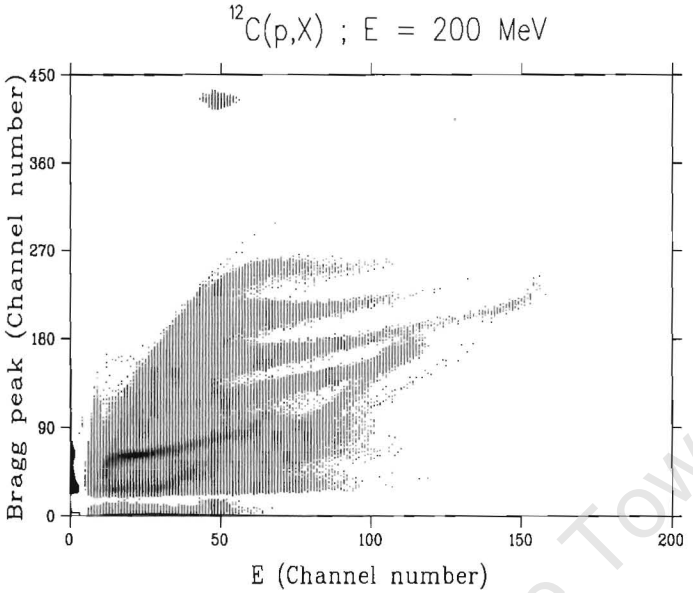

Figure 2.13: *PID obtained from the first test of the BCD with the original design.*

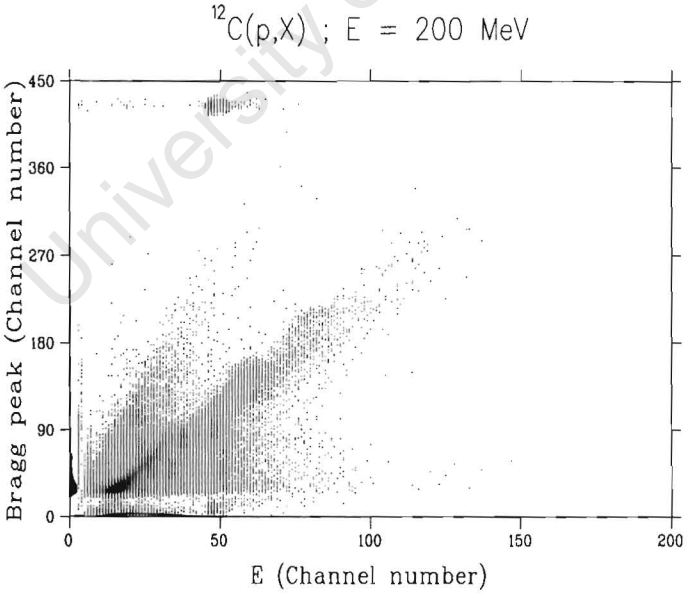

Figure 2.14: *PID spectrum obtained after the entrance window foil of the BCD was damaged.*

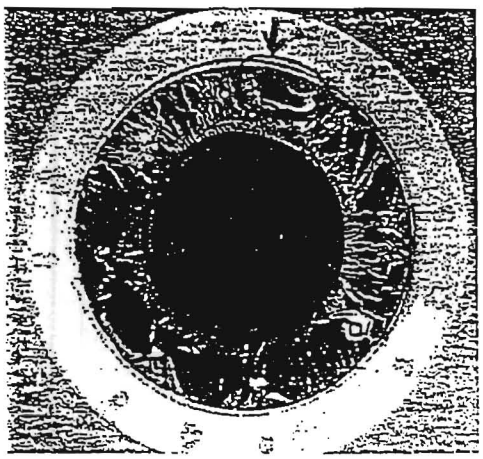

Figure 2.15: *A picture showing the damage of the aluminized mylar foil around the copper contact as indicated by an arrow.*

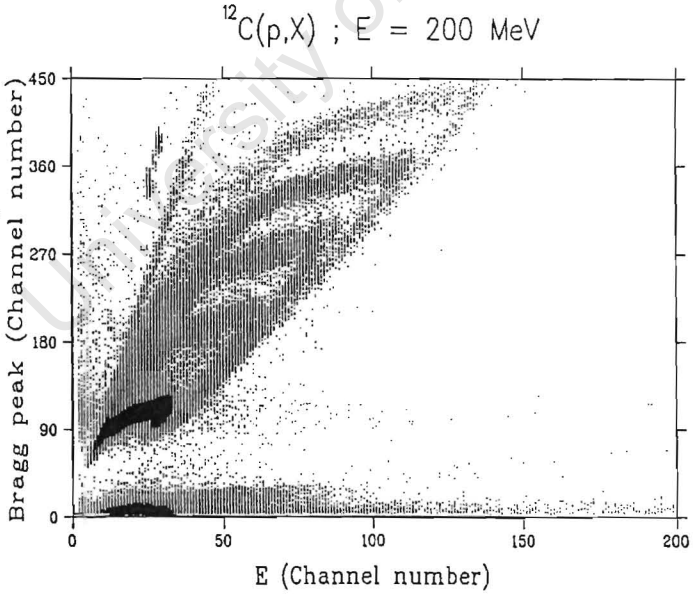

Figure 2.16: *PID spectrum obtained after the pressure was reduced to 100 mbar for the confirmation of the entrance window foil damage. At lower pressure and dynamic range of the BCD, the signals were found to have Bragg information.*

changed to be +2500 V and +1800 V respectively while the entrance window and the protective grid (cathode) were grounded. A similar design has been described by Ochiishi et. al. [Och96]. These modifications resulted in the BCD functioning excellently. All the data presented here were acquired after these modifications were made to the BCD.

Chapter 3

Analysis

Inclusive spectra of the light mass fragments in proton-induced reaction on ^{12}C at 200 MeV were measured with a BCD. The PID spectrum measured showed an excellent atomic charge (Z) separation (see section 3.4). This analysis specifically focuses on the (p,α) reaction. The double differential cross sections for energy and angular distributions of the α-particles were extracted from the PID spectrum.

3.1 Software

The software package used for the data acquisition and event data replay is called XSYS [Yod94, Pil96]. The software package XSYS runs under the VAX/VMS operating system. The actual data acquisition is controlled by the sorting sub-process called XSORT [Pil96]. It reads both the VME and the Event Analysis Language (EVAL) files. The EVAL code [Gou83] provides a language used for sorting the data either online or from event-by-event data files.

3.2 Data Acquisition

Before taking data the following steps need to be taken:

- run XSYS,
- load VME files,

- run COM file,
- and finally load EVAL file.

The VME files are used to link the communication between the different CAMAC modules like e.g. ADCs, Scaler module, event trigger module with the data acquisition system. The data are handled by XSYS that run with two files, namely the COM and the EVAL files. The COM file defines all the data areas for all the histograms to be stored including the data areas for the gates. The EVAL code uses these data areas created in the COM file to sort and analyse the raw data from the buffers. The event-by-event data is stored on the VAX computer or magnetic tape as event files, which can be replayed later during offline sorting.

3.3 Online Data Taking

Once the beam was delivered to the A-line scattering chamber the first procedure of online data taking was to align the beam to the target by centering the beam spot on the ruby target. As soon as the beam spot is aligned to the target the beam halo was reduced using an empty target frame by monitoring the BCD count rate. The background of less than 10% was accepted. Thereafter, the beam was switched onto the ^{12}C target. Before starting the data acquisition, the raw signals from the spectroscopy amplifier were first inspected on an oscilloscope to check the pulse shape of the Bragg curve. A typical shape that represent the Bragg curve from the spectroscopy amplifier as seen on the oscilloscope is shown in Figure 3.1 while the digitized Bragg curve from the flash ADC is shown in Figure 3.2. The tail of this pulse is in the electronic noise. Therefore, different isotopes could not be resolved.

The next procedure was to start the data acquisition. This is done by following the procedure explained in section 3.2. Preparations were then made to acquire the experimental data in the reaction of 200 MeV protons with ^{12}C target. The data for each run were acquired in a period of about 2 hours and collected over two weekends.

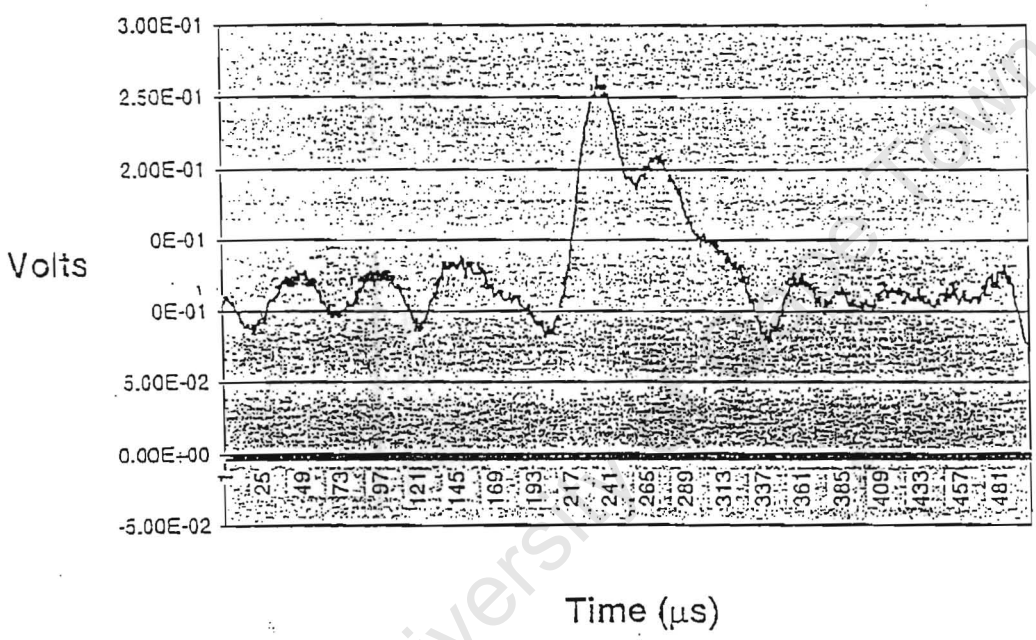

Figure 3.1: *A typical shape of the Bragg curve from the spectroscopy amplifier as seen on the oscilloscope. The shaping time of the amplifier was set to be 0.25 μs.*

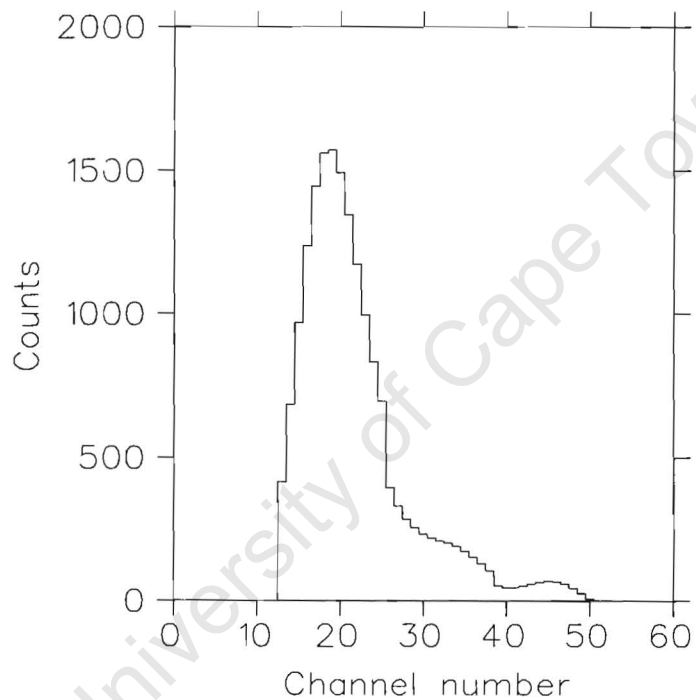

Figure 3.2: *A digitized Bragg curve from the flash ADC. The counts represent the voltage while the channel numbers represent the time.*

3.4 Particle identification

The plot of Bragg peak against energy yields a particle identification (PID) spectrum shown in Figure 3.3, where different loci of the spectrum represent Z of the light mass fragments in the range of $2 \leq Z \leq 6$. The atomic numbers of the ions were identified using a PID spectrum (Figure 2.6.3), by referring to the locus formed by the α particles measured separately using a ^{228}Th source. At the end of each locus a tailing effect is visible which is explained in section 3.8. The pulser which appeared in the PID spectrum was used for the electronic dead time determination. The PID spectrum measured with the flash ADC method is shown in Figure 3.4. Different preamplifiers were used in these two methods. Due to the higher sensitivity to noise of the preamplifier used in the flash ADC method the α signals were inside the electronic noise level. Therefore, the threshold in the discriminator had to be set in such way which excluded the α signals. Both methods could not separate different isotopes mainly due to the high levels of electronic.

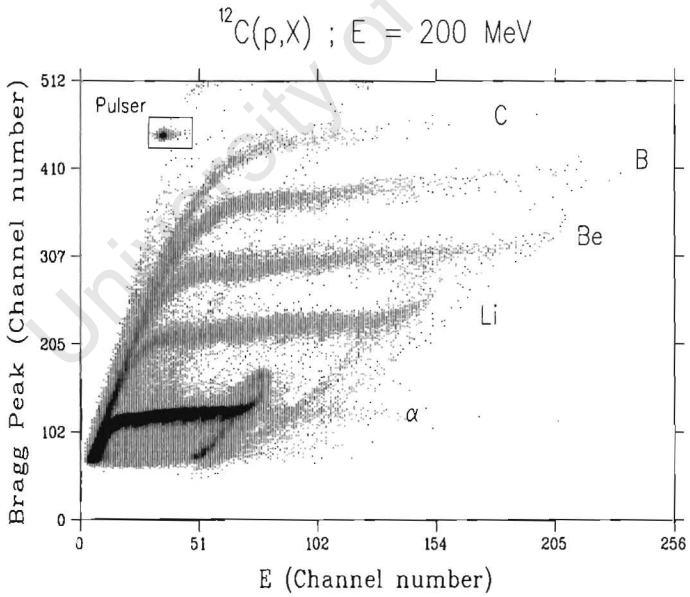

Figure 3.3: *Particle identification spectrum obtained with 2 ADC method, where X = α, Li, Be, B and C. The upwards and downwards sloping in the loci is explained in section 3.8.*

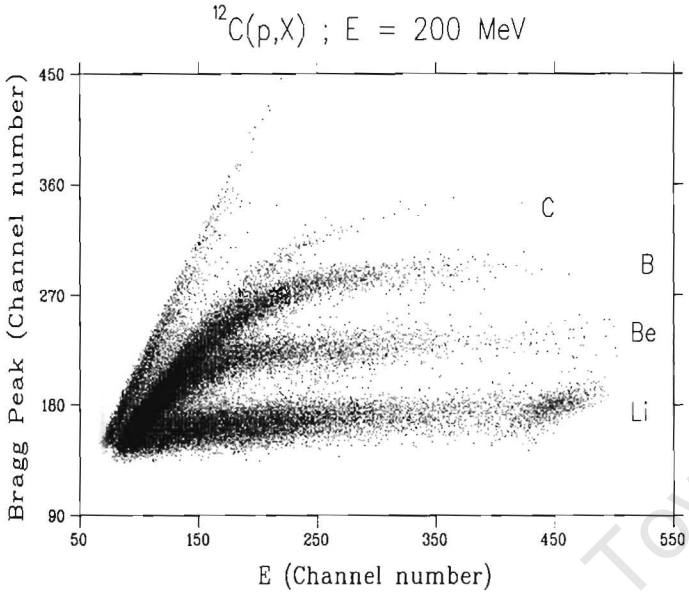

Figure 3.4: *Particle identification spectrum obtained with the flash ADC method, where X = Li, Be, B and C.*

3.5 Energy calibrations

Figure 3.5 shows an α spectrum from a ^{228}Th, which was measured with the Bragg curve detector. A Bragg curve detector is designed mainly to detect the heavier fragments. Since α particles are relatively light fragments, a Bragg curve detector is less suitable to detect their full energy spectra. The α energy spectrum from the ^{228}Th source is shown in Figure 3.5 which indicates that the Bragg curve detector could only resolve the 8.78 MeV energy peak. The other groups of peaks in the α energy spectrum from the ^{228}Th source is a combination of the energy peaks between 5 and 6 MeV which were not resolved. The energy calibration of the detector was performed by identifying the 8.78 MeV α-particle peak in relation to its corresponding channel number. A linear relationship between the channel number and energy was assumed for the energy calibrations.

Since a particle loses energy in the entrance window, its energy loss needs to be corrected for. The energy loss of the alpha-particles in the window were corrected by identifying the energy from the spectra shown in Figure 3.5 as the

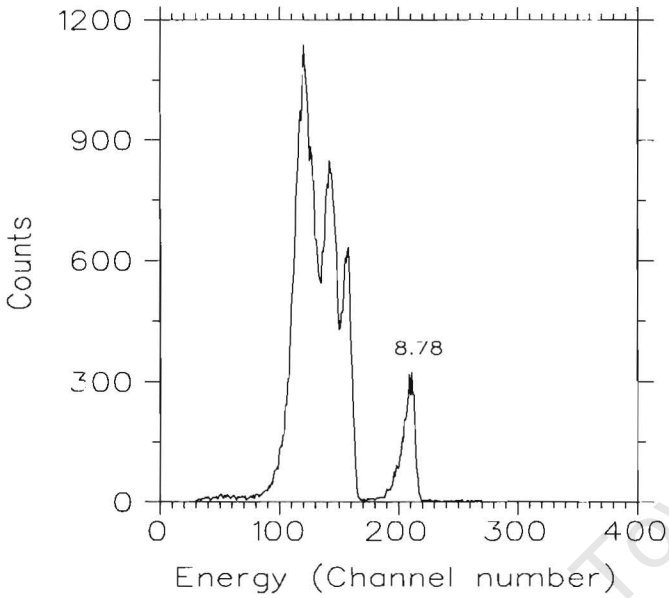

Figure 3.5: *The α spectrum from a ^{228}Th source measured with a Bragg curve detector used for the energy calibrations.*

same energy from the original source spectrum. The energy loss was calculated by the program ELOSS [Jip84]. The same energy calibration for the analysis of the other fragments (Li, Be, B and C) would be used.

3.6 Data replay

The same software used for the data acquisition was also used during data replay (section 3.3). The COM and EVAL files used during data acquisition were modified for data replay by adding more data areas for the gates and the histograms and by substituting the parameters determined from the energy calibrations. Subsequent to the necessary modifications in the COM and EVAL files the normal procedure for offline sorting similar to the data acquisition procedure were followed, in order to replay the raw data. The energy spectra for different fragments were deduced from the PID spectrum shown in Figure 3.3, by setting a 2-dimensional gate on each locus. The uncalibrated and calibrated energy spectra have a pronounced broad peak nearly at the end of the spectra. This peak is caused by tail events. The origin of these events and how to correct for them is discussed in section 3.8.

3.7 Background Subtraction

The background spectra were measured by using the empty frame target. The background was less than 10% at the most forward angles, and less than 5% at backward angles. The spectra were analysed in the same way as the inclusive spectra. The background spectra were normalized to account for the same current integrator scaler value as the inclusive spectra, so that the background can be subtracted accordingly.

3.8 Subtraction of Tail Events

The maximum energy of an α particle that can be stopped in a 16 cm active volume of the Bragg curve detector operated at 300 mbar isobutane is about 12 MeV. If an α particle has an energy higher than 12 MeV it punches through the detector. Since they are not stopped in the detector, they only deposit part of their energy in the detector, creating a fold back in the PID spectrum (see Figure 3.3). Some of the events fold up in the PID spectrum, especially in the α locus. These are caused by low energy protons that stop very close to the Frisch grid, thereby creating distorted signals which stop the linearity between the atomic number and the Bragg peak.

The fold back in the PID spectra, especially on the α locus causes a sudden broad peak to the energy spectra. This broad peak is between channel numbers 250 and 300 as shown in Figure 3.6. As shown in Figure 3.6, the effect is more severe at the most forward angle, that is 30° and is found to decrease with increasing emission angle.

The corrections of the tail events were performed in XSYS during data replay for every measured spectrum. Several stages were followed in order to correct for their contribution to the energy spectra. The first stage is to subsequently set three 2-dimensional gates on the PID spectrum as shown in Figure 3.7. By subtracting the data of gate 3 from the data of the gate 2, the spectra containing the fold back events were obtained. It was assumed that the distribution of the fold back events is linear. A linear function was used to interpolate between the events which

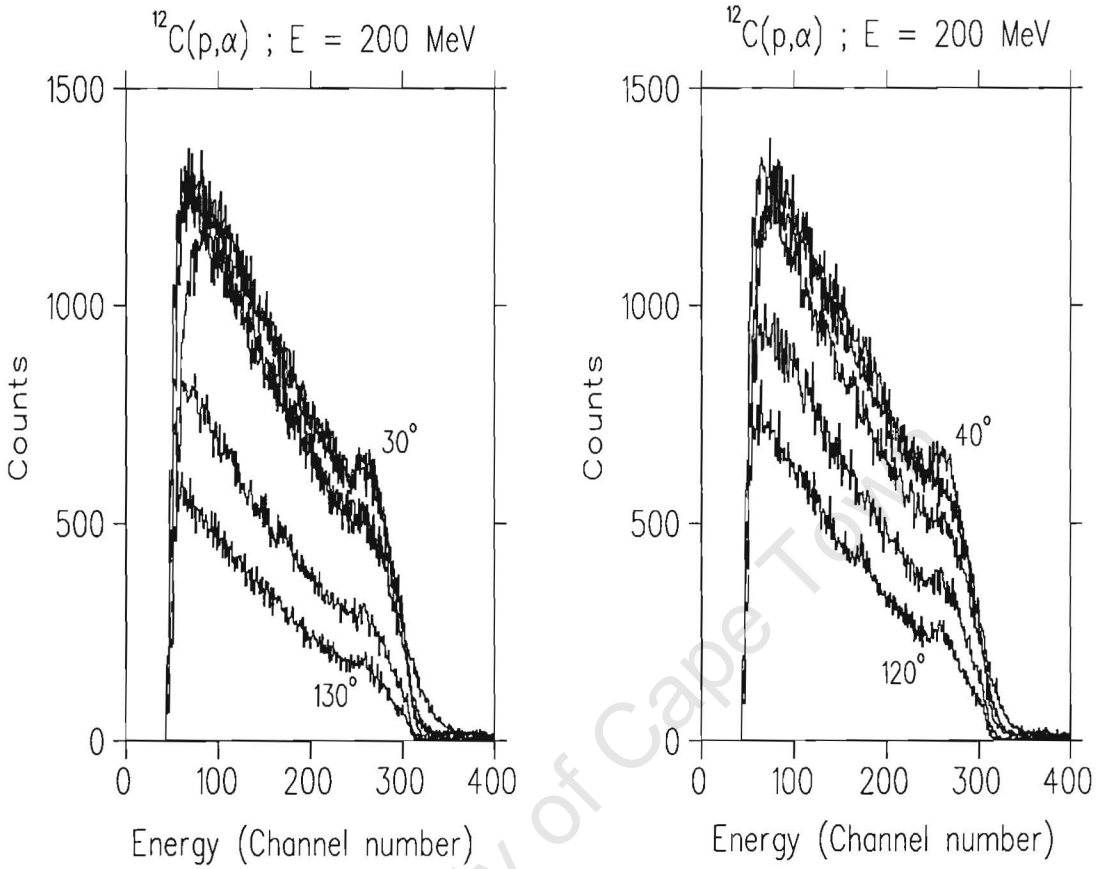

Figure 3.6: *Spectra showing tail events distribution for different lab emission angles, (a) at 30°, 50°, 70°, 90°, 110° and 130°, (b) at 40°, 60°, 80°, 100° and 120°.*

represents the shape of the tail. The last stage is to read back data from gate 1 (2-D) and subtract these from the interpolated linear function. Figure 3.8 shows the corrected energy spectrum as well as the tail distribution spectrum.

3.9 Error Analysis

3.9.1 Statistical Error

The statistical error was based on the uncertainties in the counting rate. The statistical error for the number of counts C in each bin was $\sqrt{C}$. It was calculated in XSYS during data replay. The propagation of the statistical error for the

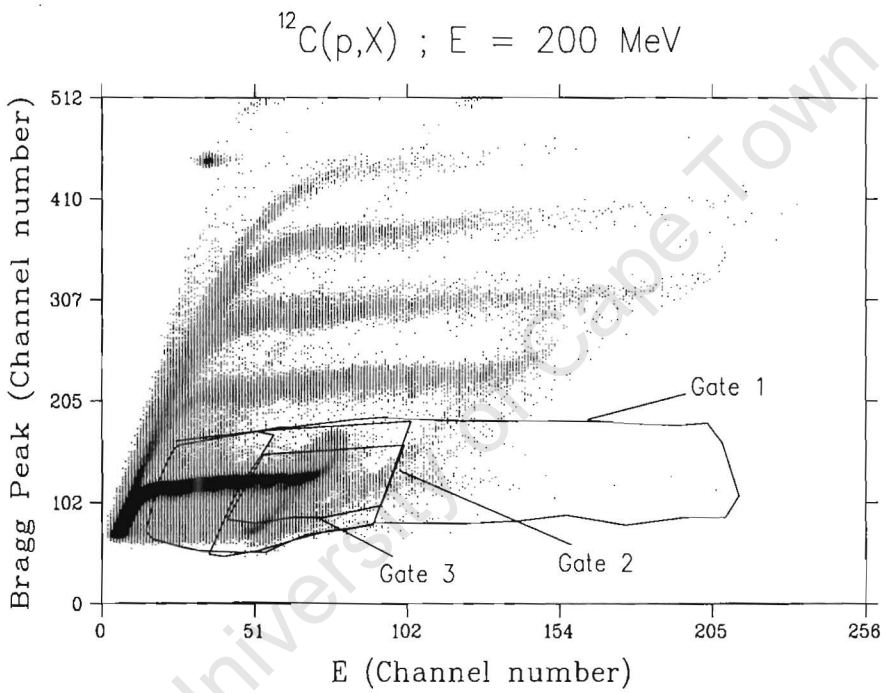

Figure 3.7: *A PID spectrum showing how three 2-D gates were set on the α locus in order to subtract tail events from the energy spectra.*

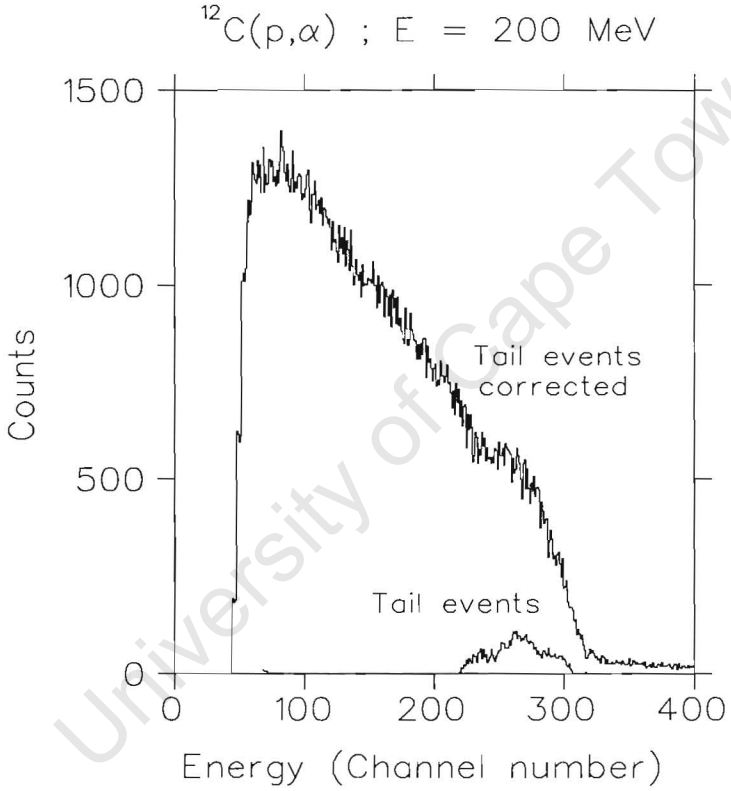

Figure 3.8: *A figure showing the tail event subtracted energy spectrum and fold back (tail) event distribution function.*

background subtractions and tail corrections were automatically performed in XSYS during data replay. The statistical error is represented by the error bars in the double differential cross sections.

3.9.2 Systematic Error

The estimated systematic error for the double differential cross section consists of contributions from the uncertainty in target thickness, solid angle, current integrator, energy calibration and particle identification. Table 3.1 summarizes the systematic errors as well as the total systematic error.

Solid angle

The uncertainty of the solid angle is due to uncertainties in the radius of the collimator and the distance between the target centre and the collimator. The maximum uncertainty in the solid angle is found to be 0.5%.

Target thickness

The uncertainty in target thickness is estimated to be 5%.

Particle identification

The largest uncertainty in the particle identification is due to the fact that the ^{3}He and α could not be separated. The α locus contains the events which are also coming from (p,^{3}He). The contributions from (p,^{3}He) were estimated to be 10 - 30% by comparing the (p,α) yield with respect to the yield of the (p,^{3}He) from the measurements performed previously at 200 MeV [Cha99].

Energy calibrations

The uncertainty in the energy calibrations resulted from the energy loss of the α-particles on the entrance window. The energy loss was taken into account to the α calibrated spectrum by either identifying an 8.78 MeV peak as from the original source spectrum or by using ELOSS program. By comparing the two methods the error was estimated to be less than 1%.

Current Integrator

The uncertainty in the current integrator was estimated to be less than 0.2%.

Table 3.1: *Summary of the systematic errors.*

Cause of systematic error	*Error in %*
Solid angle	0.5
Target thickness	5.0
Energy calibration	< 1.0
Particle identification	10-30
Current integrator	0.2
Total systematic error	10-30

3.10 Inclusive (p, α) Cross Sections

The spectra which contained the inclusive data, were converted to double differential cross sections (in b.sr^{-1}.MeV^{-1}) [För92]

$$\frac{\partial^2\sigma}{\partial\Omega\ \partial E} = N_C \cdot \Lambda \tag{3.1}$$

where

$N_C \equiv$ is the corrected number of counts in an energy bin,

and the conversion factor Λ was calculated from:

$$\Lambda = \frac{1}{\Delta\Omega\ \Delta E}\ \frac{e\ \cos\theta_T\ A}{C\ \lambda_T\ N_A\ D} \tag{3.2}$$

where

$\Delta\Omega \equiv$ is the solid angle (sr)

$\Delta E \equiv$ is the width of the energy bin (in MeV),

$e \equiv$ is the proton charge,

$D \equiv$ is the correction factor for the electronic dead time,

$\rho \equiv$ is the density of target nuclei (in b^{-1}),

$C \equiv$ is the total integrated charge as measured by current integrator at beam stop (in Coulomb), which was calculated from:

$C = CI \cdot R \cdot 10^{-12}$,

where

$CI \equiv$ is the scaler read-out of the Current integrator,

$R \equiv$ is the selected range (in nA) which represents 1000 counts·s^{-1} for a full scale current read-out, and ρ is given by:

$$\rho = \frac{\lambda_T\ N_A}{\cos\theta_T\ A} \tag{3.3}$$

where

$\lambda_T \equiv$ is the the target thickness expressed in mass per unit area,

$N_A \equiv$ is the Avogadro's number,

$\theta_T \equiv$ is the angle of the target's normal with respect to the beam direction, and

$A \equiv$ is the atomic mass of the target.

Chapter 4

Results and Discussion

4.1 Overview

Double differential cross sections of energy and angular distributions for the emission of the light mass fragments ($2 \leq Z \leq 6$) from the ^{12}C(p, X) reaction at 200 MeV were measured with a BCD down to emission energies as low as about 1 MeV/amu over an angular range of 30^0 to 130^0. The PID plot of Bragg peak height (~atomic number) vs. kinetic energy of light mass fragments detected by BCD are shown in Figure 3.3. Here, only the double differential cross sections of energy and angular distributions of the α-particles which were obtained from the PID plot (Figure 3.3) are presented. The measured angular distributions spectra were fitted with calculated angular distributions based on the Kalbach systematic parameterizations. The comparison between the Bragg curve spectroscopy (BCS) and ΔE-E techniques as well as the two techniques used to acquire the data will also be presented in this Chapter.

4.2 (p, α) Continuum spectra

4.2.1 Energy spectra

Figure 4.1 shows the full energy spectrum measured with the BCD and the standard ΔE-E technique using Si(ΔE) and NaI(E) detectors. The low-energy cutoff at about 20 MeV in the ΔE-E telescope arises from the detector thresholds. To

avoid such a low-energy threshold, a BCD with a thin entrance window was used. The gap between these two spectra lies beyond the energy response of the BCD and ΔE-E detectors. Since the BCD operates at a pressure of about 300 mbar it could only measure the energies of alphas up to a maximum of 12 MeV, while the ΔE-E detectors could measure the full energy spectrum from a minimum of about 20 MeV.

The energy distribution spectra of the alphas for the reaction of 200 MeV protons on ^{12}C at different lab angles are presented in Figure 4.2. The energy distributions follow an exponential shape. In the angular range of 30° to 60° the cross sections are quantitavely very similar. As mentioned in section 1.1, the Bragg signals were processed with two techniques. The comparison of these two techniques are presented in Figure 4.3, in which they give consistent results.

4.2.2 Angular distributions

The α angular distributions are shown in Figure 4.4 for three emission energies, i.e. 4, 6 and 8 MeV. Double differential cross section calculations based on the Kalbach systematic parameterization [Kal88] were fitted to these spectra. The results of these calculations are shown in sections 4.3.3 and 4.3.4.

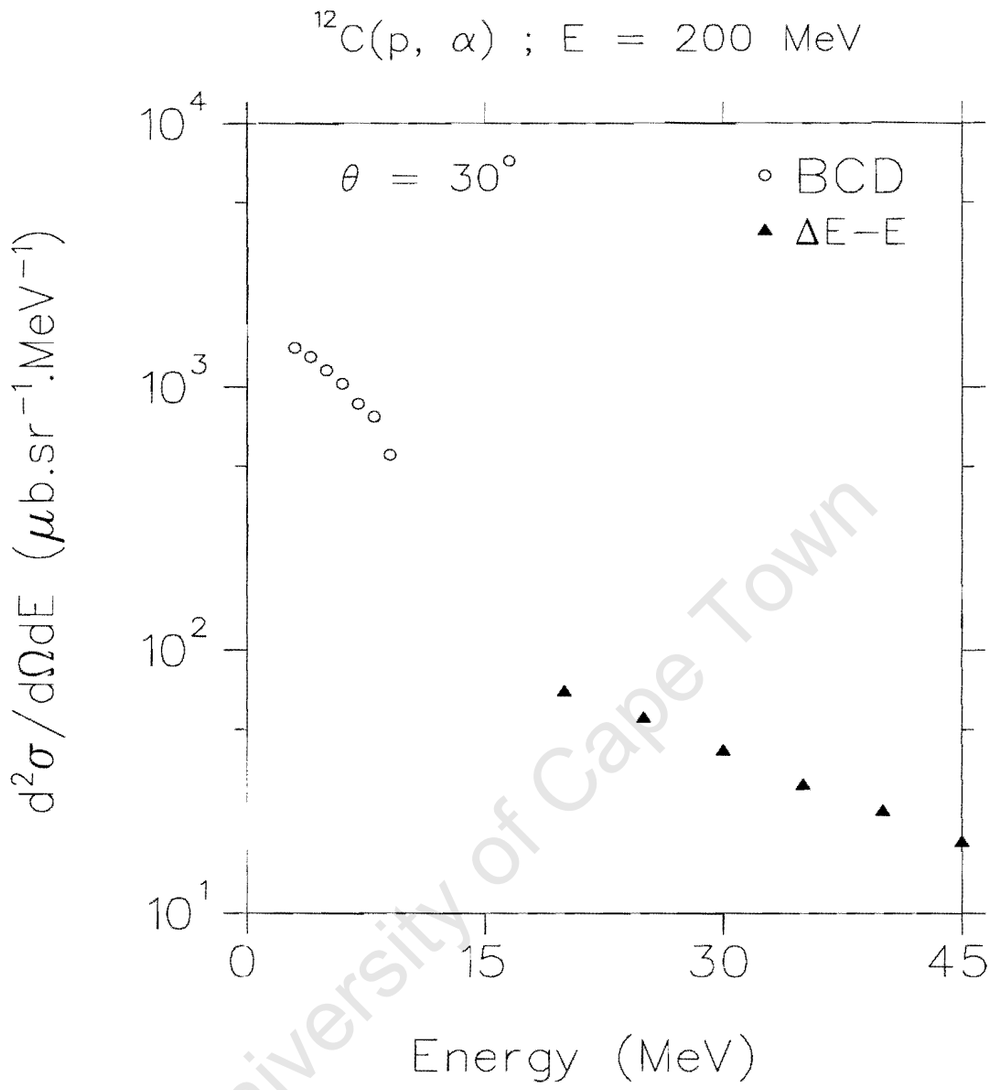

Figure 4.1: *An α energy spectrum from the reaction of 200 MeV protons on ^{12}C (open circles) is added to the existing data (solid triangles) previously measured with a ΔE-E telescope as displayed.*

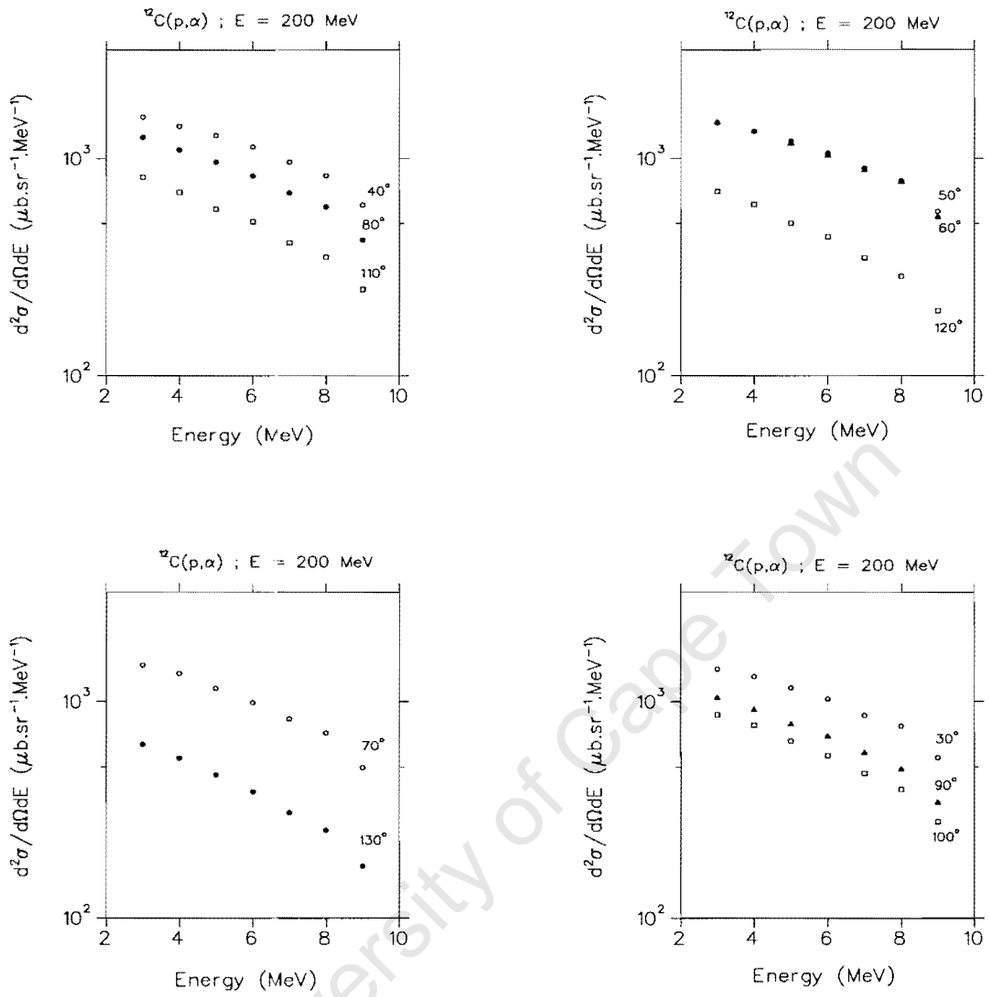

Figure 4.2: *Double differential cross sections of the alphas emitted from the reaction of 200 MeV protons on ^{12}C at different lab emission angles as indicated.*

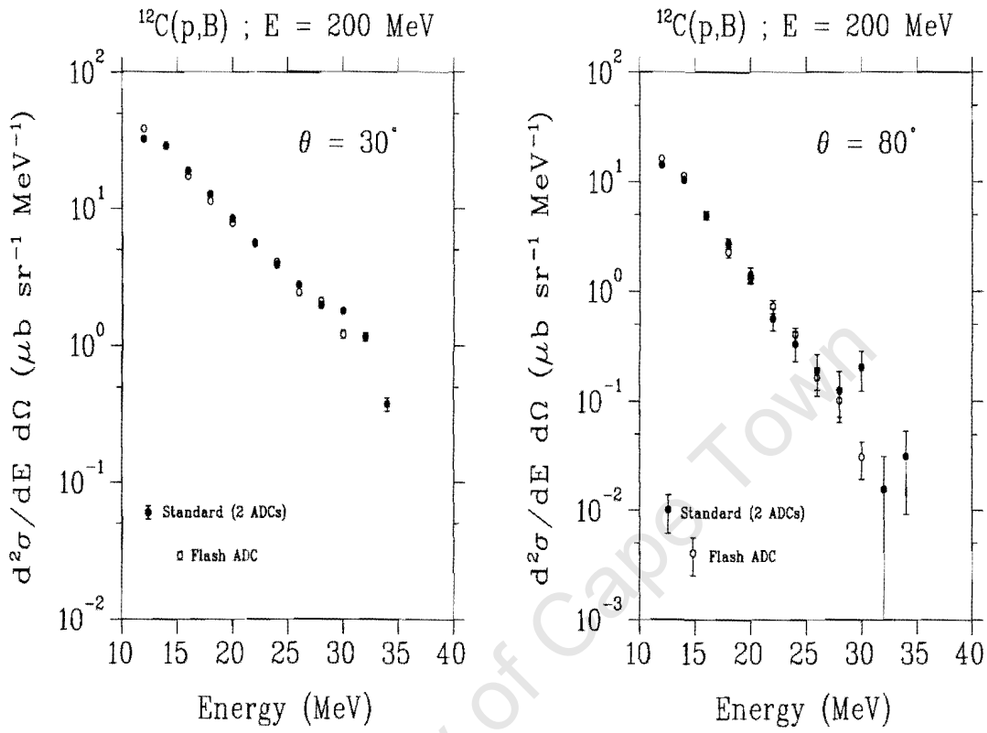

Figure 4.3: *Cross sections of Boron nuclei emitted in the reaction of 200 MeV protons on ^{12}C. Results sampled with the flash ADC, are given by the open symbols, while data obtained from 2 ADCs, solid symbols. The error bars shown here are only statistical errors.*

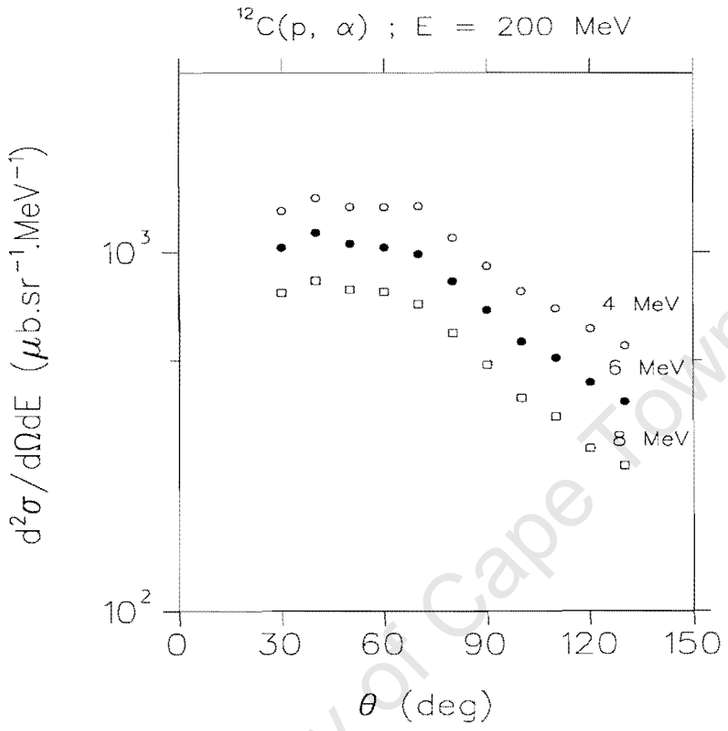

Figure 4.4: *Double differential cross sections of the alphas emitted from the reaction of 200 MeV protons on ^{12}C at emission energies of 4 MeV, 6 MeV and 8 MeV as indicated.*

4.3 Kalbach Systematic Parameterizations

4.3.1 Introduction

The Kalbach systematics were first aimed to describe the shapes of continuum angular distributions for inclusive reactions at incident energies up to 80 MeV and emission energies up to 60 MeV [Kal81]. Later they were extended to higher incident energies exceeding even 200 MeV [Kal88]. The angular dependence of the inclusive cross section was, at least to first order, to be independent of the bombarding energy and the nature of the projectile, target, and emitted particle. The systematics were parameterized in terms of Legendre polynomials up through order 6 using only a small number of universal parameter. All of the polynomials contribute to the multistep direct component while only the even order polynomials are used for multistep compound processes.

The distinction between MSC and MSD reactions described in section 1.2.2 was subsequently used by Kalbach and Mann [Kal81] in their empirical parameterizations of pre-equilibrium cross-sections. This parameterization of the (p,α) reaction of 200 MeV protons on ^{27}Al [Kal88] shows that the angular distributions of the 80 MeV α particles are found to be dominated by a MSD process. Since Al is a light target close to C, the aim of this study is to establish whether the angular distributions at low emission energies can still be analysed by a pure MSD formalism and what role do possible MSC contributions to the cross sections play using the Kalbach parameterizations.

4.3.2 Continuum angular distributions

The general mathematical expression of both MSD and MSC for the angular distributions in the center of mass system is given by [Kal88]

$$\left.\frac{d^2\sigma}{d\Omega d\epsilon_b}\right|_{cm} = \frac{1}{4\pi}\frac{d\sigma}{d\epsilon_b}\frac{a}{\sinh(a)}[\cosh(a\cos\theta) + f_{MSD}\sinh(acos\theta)] \qquad (4.1)$$

where

$\epsilon_b \equiv$ *ejectile energy of an* α *particle*

$\frac{d\sigma}{d\epsilon_b} \equiv$ *angle integrated cross section*
$f_{MSD} \equiv$ *fraction of the cross section due to MSD process*
$\theta \equiv$ *emission angle in centre-of-mass*
$a \equiv$ *slope parameter*

The angle integrated cross section ($\frac{d\sigma}{d\epsilon_b}$) and the fraction, f_{MSD}, is assumed to be known from preequilibrium calculations or from experiment. In this experiment, the values of $\frac{d\sigma}{d\epsilon_b}$ for each emission energy were determined experimentally by normalizing the calculated angular distributions to the measured angular distributions.

Since equation 4.1 is expressed in the centre of mass frame the calculated cross sections were converted into the laboratory frame in order to be fitted to the data. The conversions were performed by dividing equation 4.1 by a relative Jacobian. These conversions were necessary since the reaction kinematics between the entrance and exit channel of the reaction ^{12}C(p, α)^{9}Be are quite different. The relative Jacobians were obtained from the kinematic calculations over an angular range of 30^o to 130^o in 10^0 steps. Table curve program [SPS01] was used to fit the curve to these values in order to obtain the expressions to calculate the relative Jacobian in 1^0 steps for each emission energy of the α particle. The list of the parameters together with their values are listed in Table 4.1. The relevant expressions for each emission energy are summarized as follows:

(i) Relative Jacobian for 4 MeV

$$J_R(\theta_{cm}) = \sqrt{a_1 \; + \; b_1 \; \frac{\ln \theta_{cm}}{\theta_{cm}^2}} \tag{4.2}$$

where,
J_R is Relative Jacobian,
θ_{cm} is emission angle in centre of mass given by

$$\theta_{cm} = a_2 \; + \; b_2 (\ln \theta_{lab})^2 \tag{4.3}$$

and θ_{lab} is the emission angle in laboratory frame.

(ii) Relative Jacobian for 6 MeV

$$J_R(\theta_{cm}) = \exp\left(a_3 + \frac{b_3}{\theta_{cm}}^2\right) \tag{4.4}$$

$$\theta_{cm} = [a_4 + b_4 \ (\ln\theta_{lab})^2]^2 \tag{4.5}$$

(iii) Relative Jacobian for 8 MeV

$$J_R(\theta_{cm}) = a_5 + b_5 \ \exp\left(\frac{-\theta_{cm}}{c}\right) \tag{4.6}$$

$$\theta_{cm} = a_6 + b_6 \ \exp\left(\frac{-\theta_{lab}}{c_1}\right) \tag{4.7}$$

Finally, the equation 4.1 becomes

$$\left.\frac{d^2\sigma}{d\Omega d\epsilon_b}\right|_{lab} = \frac{1}{J_R(\theta_{cm})} \cdot \left.\frac{d^2\sigma}{d\Omega d\epsilon_b}\right|_{cm} \tag{4.8}$$

In this case, the calculated angular distributions were performed only for two f_{MSD} factors, namely $f_{MSD} = 1$ and $f_{MSD} = 0$. The factor $f_{MSD} = 1$ represents 100 % MSD contribution to the double differential cross sections while the factor $f_{MSD} = 0$ represents 100 % MSC contribution to the double differential cross sections.

The calculated angular distributions were normalized to the experimental angular distributions. The normalization factor corresponds to the angle integrated cross section ($\frac{d\sigma}{d\epsilon_b}$). The normalization factor related to the MSD process is found to be different to the MSC process. These normalization factors are compared in Table 4.2 with the predicted values calculated using code ALICE [Bla84a] based on the geometry-dependent hybrid model [Bla84b].

4.3.3 Multistep Direct ($f_{MSD} = 1.0$)

The angular distribution results for $f_{MSD} = 1.0$ are shown in Figure 4.5. The results do not agree with the experimental data due to the fact that at low emission energies the influence of the multistep direct process is not expected to play a

Table 4.1: *List of parameters and their values used to calculate the relative Jacobians in eq. 4.2 - 4.7.*

Parameters	*Values*
a_1	4.2110985
a_2	-155.73599
a_3	3.1809554
a_4	-22.03385
a_5	-0.37983063
a_6	-88.434533
b_1	-11574.323
b_2	-6.9472138
b_3	-50747.449
b_4	1.3188209
b_5	0.063975228
b_6	57.959276
c	-40.132009
c_1	-115.73906

Table 4.2: *Comparison of predicted and experimental* $\frac{d\sigma}{d\epsilon_b}$ *values for the reaction induced by 200 MeV protons on* ^{12}C*, where* ϵ_b *is the emission energy of the* α *particle.*

ϵ_b *(MeV)*	$\frac{d\sigma}{d\epsilon_b} \mid_{MSC}$ $(mb.MeV^{-1})$	$\frac{d\sigma}{d\epsilon_b} \mid_{MSD}$	$\frac{d\sigma}{d\epsilon_b} \mid_{ALICE}$
4	18	58	4.603
6	11.5	36	3.661
8	9.2	22	2.868

significant role in the reaction mechanism [Gad92]. A previous study [Cow96] of the (p,α) reaction with 120, 160 and 200 MeV protons on ^{27}Al indicates that the angular distributions of the cross sections of the α particles were found to be dominated by MSD process at higher emission energies.

4.3.4 Multistep Compound ($f_{MSD} = 0.0$)

The angular distribution results for $f_{MSD} = 0.0$ are also shown in Figure 4.5. The results agree significantly better with the experimental data, especially at the large angles. The MSC contributions to the cross sections are most prominent in the low emission energy region. At very low emission energies, the parameterization is expected to be nearly purely MSC. It seems not to be the case, since the parameterization do not fit well at most forward angles. However, Kalbach [Kal88] mentions that this parameterization may not behave well in the low energy.

Figure 4.6, represents the energy distributions of angle integrated cross sections calculated with the code ALICE compared to the values obtained from the normalizations of the Kalbach parameterizations to the experimental data. ALICE calculations predict smaller values for the angle integrated cross sections compared to the MSC and MSD values. This discrepancy could be due to the fact that the α cross sections are contaminated with ^{3}He by an estimated amount of between 10 to 30%. Hence, the MSC and MSD angle integrated cross sections also include ^{3}He contributions. The angle integrated cross sections from (p,p') data [För91] agree

reasonably well with the predicted values from ALICE. Since then the ALICE code was improved to such an extent that it can calculate the double differential cross sections which agree well with data of (p,xp') and (p,xn) [Bla98]. It would be of great importance in future to investigate whether the ALICE code [Bla98] could also be able to calculate the double differential cross sections for the (p,α) reaction even at these low emission energies.

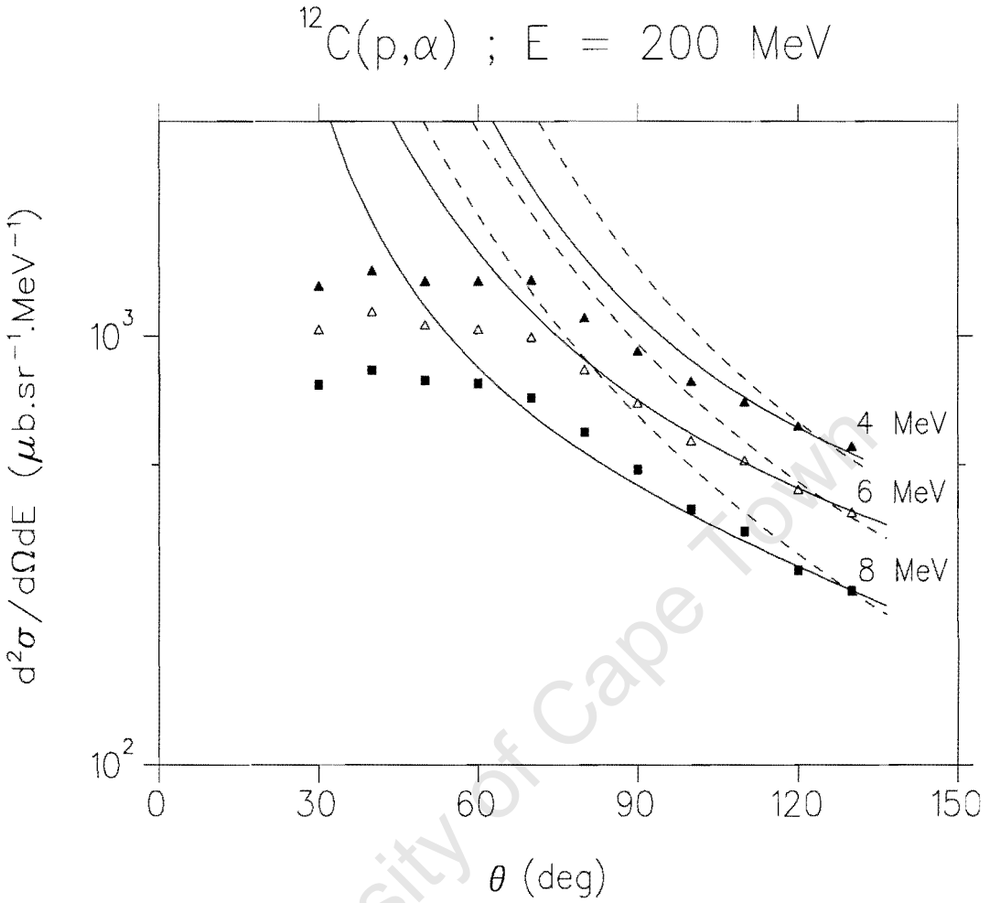

Figure 4.5: *Double differential cross sections of the alphas emitted from the reaction of 200 MeV protons on ^{12}C at emission energies of 4 MeV, 6 MeV and 8 MeV as indicated. The solid lines, dashed lines and symbols represent the MSC, MSD and experimental data, respectively.*

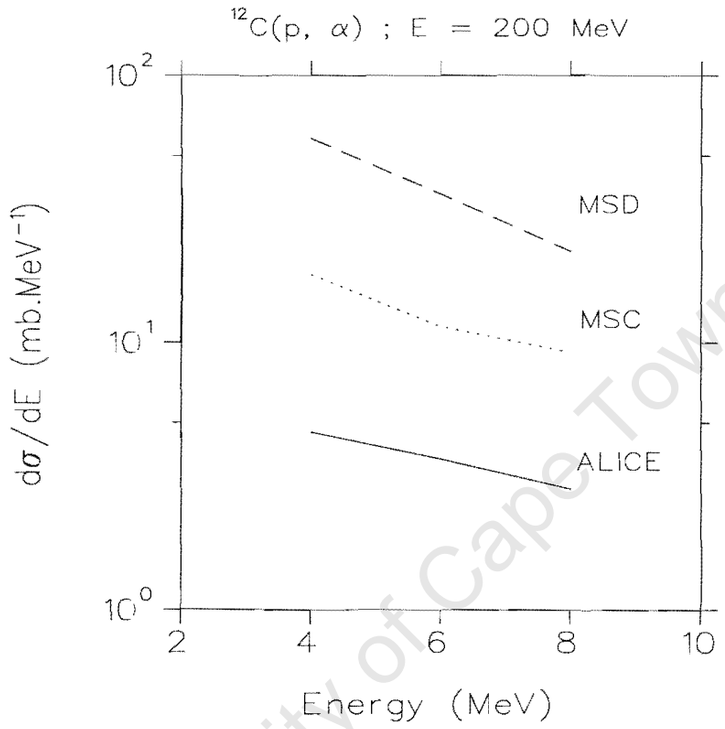

Figure 4.6: *Comparison of the experimental angle integrated cross sections (MSD and MSC) with the predicted angle integrated cross sections (Alice).*

Chapter 5

Summary and Outlook

The present study has shown that the Bragg curve detector can be employed to measure cross sections of particles with $2 \leq Z \leq 6$ emitted to the continuum from proton-induced reactions on ^{12}C at an incident energy of 200 MeV. An energy threshold of about 1 MeV/amu was achieved with this detector. The entrance window foil was found to be the main problem initially experienced with the BCD. Modifications of the entrance window foil were made, which resulted in the BCD functioning reasonably well. Most importantly, the data read out was performed with two set-ups, which consisted of a flash ADC and two ADCs. The comparison of these set-ups gave consistent results. With these measurements different isotopes of the emitted fragments could not be resolved mainly due to rather high levels of electronic noise. Nevertheless, an isotopic separation was achieved for ^{7}Be and ^{9}Be. The angular distributions of the (p,α) reaction at various kinetic energies were fitted with the Kalbach parameterization. This parameterization was aimed at establishing whether the angular distributions at low emission energies can still be analysed by a pure MSD formalism, and what role possible MSC contributions to the cross sections play. Kalbach parameterizations approach suggest that the α spectra at low emission energies indicate an increase in the multistep compound contribution to the cross sections.

In order to measure a full energy spectrum of a light detected particle, a combination of the Bragg curve detector with another stopping detector (like for example a silicon detector) can be used. Such a combination was also recently used in a

Proton Induced Spallation (PISA) experiment performed at COSY Jülich [COS99]. In this experiment, standard ΔE - E technique was employed by using Bragg curve detector as a ΔE detector and silicon as a stopping E detector so that the high energy particles of the light emission fragments can also be measured. Since the degree of applicability of a Bragg curve detector depends mostly on the Frisch grid to anode gap and the thin entrance window, a Bragg curve detector with shorter Frisch to anode gap can be employed so that particles with higher charge and low energies can be detected. A BCD dedicated for measuring fission fragments of ^{252}Cf is presented by Oed et. al [Oed83] where the energy resolution for the heavier fragments were found to be better than the energy resolution of a surface barrier detector by a factor of at least 3.

In order to optimize the efficiency of the Bragg curve detector further, the next phase of this project includes the reduction of the thickness of the entrance window by applying a thinner carbon layer as well as the introduction of a charge sensitive preamplifier specifically designed for a Bragg curve detector so that electronic noise can be reduced. To increase the rate of data taking the geometry consideration of a BCD can be changed by reducing its width and length so that more than one BCD can be mounted inside the A-line scattering chamber and that angles less than 30^o can be reached.

Bibliography

[And97] L. N. Andromenko, PNPI Research Report, p. 237 (1996-1997).

[Ass82] J. M. Asselineau, J. Duchon, M. L´Haridon, P. Mosrin, R. Regimbart and B. Tamain, Nucl. Instrum. Methods **204**, 109 (1982).

[Bie89] J. P. Biesack and J. K. Ziegler, Calculation from TRIM, version - 95.9 (1989).

[Bla84a] M. Blann. Code ALICE/85/300, Lawrence Livermore National Laboratory Report No. **UCID – 20169** (unpublished) (1984).

[Bla84b] M. Blann, W. Scobel and E. Plechaty, Phy. Rev. C **30**, 1493 (1984).

[Bla98] M. Blann and M. B. Chadwick, Phy. Rev. C **57**, 233 (1998).

[Bot90] A. S. Botvia, Nucl. Phys. A **507** 649 (1990).

[Bun47] O. Bunemann, T. E. Cranshaw and J. A. Harvey, Canadian Journal of Research, Vol. **27**, Section **A** (1947) 191.

[CAE99] CAEN, Technical Information Manual (*Mod. V729A, 4-channel 12-bit 40 MHz ADC*), Revision no. 1 (1999).

[Cer92] I. Cervesato, E. Fabrici, E. Gadioli, E. Gadioli-Erba and M. Galmarini, Phy. Rev. C**45**, 2369 (1992).

[Cha99] M. B. Chadwick, D. T. L. Jones, G. J. Arendse, A. A. Cowley, W. A. Richter, J. J. Lawrie, R. T. Newman, J. V. Pilcher, F. D. Smit, G. F. Steyn, J. W. Koen and J. A. Stander, Nucl. Phys. A **654**, 1051c (1999).

[COS99] COSY Proposal No: 73 *Measurement of spallation product distributions*, see also Annual Report 1999 Institut für Kernphysik COSY p.175.

[Cow90] A. A. Cowley, S. V. Förtsch, J. J. Lawrie, D. M. Whittal, F. D. Smit, and J. V. Pilcher, Phys. A **336**, 1950 (1990).

[Cow96] A. A. Cowley, G. F. Arendse, J. W. Koen, W. A. Richter, J. A. Stander, G. F. Steyn. P. Demetriou, P. E. Hodgson and Y. Watunabe, Phy. Rev. C**54**, 778 (1996).

[Cug97] J. Cugnon, C. Volant, S. Vuillier, Nucl. Phy. A **625**, 729 (1997).

[Enk99] M. Enke, C. M. Herbach, D. Hilscher, U. Jahnke, O. Schapiro, A. Letourneau, J. Galin, F. Goldenbaum, B. Lott, A. Péghaire, D. Filges, R. -D. Neef K. Nünighoff, H. Schaal, G. Sterzenbach, A. Tietze, L. Pienkowski, Nucl. Phy. A **657**, 317 (1999).

[Far94] K. A. Farrar, A. T. Hasan, F. W. Prosser, S. J. Sanders and D. J. Henderson, Nucl. Instr. Meth. A **346**, 177 (1994).

[Fes80] H. Feshbach, A. K. Kerman, S. Koonin, Ann. Phys. **125**, 429 (1980).

[Fes92] H. Feshbach, Theorical Nuclear Physics, (John Wiley and sons, New York, 1992).

[Fes93] H. Feshbach, Phys. Rev. C **48** R2553 (1993).

[Fes95] H. Feshbach, Nucl. Phys. News, Vol. 5, No. 1, (1995).

[För91] S. V. Förtsch, A. A. Cowley, J. J. Lawrie, D. M. Whittal, J. V. Pilcher, and F. D. Smit, Phy. Rev. C**42**, 691 (1991).

[För92] S. V. Förtsch, Proton emission in pre-equilibrium reactions induced by protons of 100 and 200 MeV, Ph.D. thesis (1992), University of Pretoria (Unpublished).

[Gad92] E. Gadioli, and P. E.Hodgson, Pre-Equilibrium Nuclear Reaction, (Clarendon Press, Oxford, 1992).

[Gom74] J. Gomez del Campo, J. L. C. Ford, R. L. Robinson, P. H. Setelson and S. T. Thornton, Phys. Rev. C **9**, 1258 (1974).

[Gou83] C. R. Gould and N. R. Roberson, IEEE Trans. Nucl. Sci. **NS – 30**, 3758 (1983).

[Gru82] C. R. Gruhn, M. Binimi, R. Legrain, R. Loveman, W. Pang, M. Roach, D. K. Scott, A. Shotter, T. J. Symons, J. Wouters, and M. Zisman, Nucl. Instrum. Methods A **196**, 33 (1996).

[Hod71] P. E. Hodgson, Nuclear Reactions and Nuclear Structure, (Clarendon Press, Oxford, 1971).

[Jam83] A. N. James, P. A. Butler, T. P. Morrison, J. Simpson and K. A. Connell, Nucl. Instrum. Methods **212**, 545 (1983).

[Jip84] P. Jipsen, ELOSS, A program for calculating the ranges of ions in matter, iThemba LABS (unpublished) (1984).

[Kal81] C. Kalbach, F. M. Mann, Phys. Rev. C **23**, 112 (1981).

[Kot95] A. A. Kotov, Nucl. Phys. A **583**, 575 (1995).

[Kal88] C. Kalbach, Phys. Rev. C **37**, 2350 (1988).

[Kno99] G. F. Knoll, *Radiation Detection and Measurement*, Third Ed. (John Wiley and Sons, New York, 1999).

[Lil01] J. S. Lilley, Nuclear Physics principles and Applications, (John Wiley and Sons, Ltd, 2001).

[Leo87] W. R. Leo. Techniques for Nuclear and Particle Physics Experiments, (Springer-Verlag Berlin Heidelberg, 1987).

[Mor84] A. Moroni. I. Iori, L. Z. Yu, G. Prete, F. Gramegna and A. Dainelli, Nucl. Instr. Method A **225**, 57 (1984).

[Mye66] W. D. Myers and W. J. Swiatecki, Nucl. Phys.**81**, 1 (1966).

[Och96] H. Ochiishi, H. Ito, K. Kimura, S. Kouda, T. Murakami, M. Shimooka, Y. Sugaya, K.H. Tanaka, S. Toyama, Y. Yamanoi, K. Yamamoto, K. Yasuda. Nucl. Instrum. Methods A **369**, 269 (1996).

[Oed83] A. Oed, P. Geltenbort, F. Gönnenwein, T. Manning and D. Souque, Nucl. Instr. Meth **205**, 455 (1983).

[Ort89] H. G. Ortlepp and A. Romaguera, Nucl. Instrum. Methods A **276**, 500 (1989).

[Ort98] H. G. Ortlepp, W. Wagner, C. M. Herbasch, A. A. Aleksandrov, I. A. Aleksandrova, M. Andrassy, A. Budzanowski, B. Czech, M. Danziger, L. Dietterle, V. N. Doronin, S. Dshemuchadse, A. S. Fomichev, W. D. Fromn, Nucl. Instrum. Methods A **403**, 65 (1998).

[Pil89] J. V. Pilcher, Ph.D. thesis (1989), University of Cape Town (Unpublished).

[Pil96] J. V. Pilcher, The NAC MBD to VME Conversion Guide (1996).

[Por89] N. T. Porile, A. J. Bujak, D. D. Carmony, Y. H. Chung, L. J. Gutay, A. S. Hirsch, M. Mahi, G. L. Paderewski, T. C. Sangster, R. P. Scharenberg and B. C. Stringfellow, Phy. Rev. C**39**, 1914 (1989).

[Raa87] D. A. Raavé, *The control and Auxiliary Equipment of the National Accelerator Centre Precision 1.5m Scattering Chamber, Masters Diploma in Electrical Engineering dissertation*, Cape Technikon (1987).

[Roc76] C. T. Roche, R. G. Clark, G. J. Mathews and V. E. Viola, Phys. Rev. C **14**, 410 (1976).

[She85] N. J. Shenhev and H. Stelzer, Nucl. Instrum. Methods **109**, 359 (1985).

[SPS01] Tablecurve 2D Version 5.1, SYSTAT Software, Marketed by: SPSS Inc. USA (2001).

[Tan95] K. H. Tanaka, Y. Yamanoi, H. Ochiichi, H. Akiyoshi, S. Kounda, H. Nakamura, S. Morinobu, Y. Tanaka, K. Kimura, T. Shibata, Y. Sugaya, K. Yasuda, K. Yasuda, H. Ito, and T. Murakami, Nucl. Phys. **A583**, 581 (1995).

[Tso83] N. Tsoulfanidis, Measurement and Detection of radiation, (Hemisphere Publishing Corparation, New York, 1983).

[Tra89] M. Trabandt, W. Scobel, M. Blann, B. A. Pohl, R. C. Byrd, C. C. Foster, S. M. Grimes, and R. Bonetti, Phys. Rev. C **39**, 452 (1989).

[Wes88] W. R. Wesber, J. C. Kish and D. A. Schrier, Phys. Rev. C **41** 520 (1988).

[Yod94] N. R. Yoder, IUCF VME DAta Acquisition System User Information Manual, Indiana Universiy Cycloctron Facility (1994).